

Galactic potential constraints from clustering in action space of combined stellar stream data

Stella Reino,¹ Elena M. Rossi,¹ Robyn E. Sanderson,^{2,3} Elena Sellentin,¹ Amina Helmi,⁴ Helmer H. Koppelman,⁴ Sanjib Sharma⁵

¹Leiden Observatory, Leiden University, Niels Bohrweg 2, 2333 CA Leiden, The Netherlands

²Department of Physics and Astronomy, University of Pennsylvania, 209 S 33rd St., Philadelphia, PA 19104, USA

³Center for Computational Astrophysics, Flatiron Institute, 162 5th Ave., New York, NY 10010, USA

⁴Kapteyn Astronomical Institute, University of Groningen, P.O. Box 800, 9700 AV Groningen, The Netherlands

⁵Sydney Institute for Astronomy, School of Physics, The University of Sydney, NSW 2006, Australia

Accepted XXX. Received YYY; in original form ZZZ

ABSTRACT

Stream stars removed by tides from their progenitor satellite galaxy or globular cluster act as a group of test particles on neighboring orbits, probing the gravitational field of the Milky Way. While constraints from individual streams have been shown to be susceptible to biases, combining several streams from orbits with various distances reduces these biases. We fit a common gravitational potential to multiple stellar streams simultaneously by maximizing the clustering of the stream stars in action space. We apply this technique to members of the GD-1, Pal 5, Orphan and Helmi streams, exploiting both the individual and combined data sets. We describe the Galactic potential with a Stäckel model, and vary up to five parameters simultaneously. We find that we can only constrain the enclosed mass, and that the strongest constraints come from the GD-1 and Pal 5 streams whose combined data set yields $M(< 20 \text{ kpc}) = 3.47^{+0.95}_{-1.44} \times 10^{11} M_{\odot}$. When including the Orphan and Helmi stream in the data set, the mass uncertainty increases to $M(< 20 \text{ kpc}) = 3.12^{+5.69}_{-1.07} \times 10^{11} M_{\odot}$, indicative of the hidden systematic errors in fits to individual streams. These systematics are likely due to insufficiencies in our Stäckel model of the potential and to the limited phase space explored by the data set of 4 streams, so the larger uncertainty of the combined fit is the more robust measure of the actual uncertainty in the Milky Way potential.

Key words: dark matter, Galaxy: kinematics and dynamics, Galaxy: structure, Galaxy: fundamental parameters, methods: numerical

1 INTRODUCTION

The outer reaches of the Milky Way, known as the “halo”, are dominated by dark matter. Knowledge of the mass and shape of the halo is required for placing strong constraints on the formation history of the Milky Way, testing the nature of dark matter and modified gravity models (e.g. Mao et al. 2015; Thomas et al. 2018). Some of the most promising dynamical tracers of the Galactic potential in the halo region are stellar streams. Stellar streams form when stars are torn from globular clusters or dwarf galaxies due to Galactic tidal forces. The stars in the ensuing debris gradually stretch out in a series of neighboring orbits. This property makes stellar streams superb probes of the underlying gravitational potential, allowing us to constrain the mass distribution within the extent of their orbits (Johnston et al. 1999). In addition, density variations and gaps within a stream can potentially provide information about past encounters with

small-scale substructure and therefore an opportunity to detect the presence of dark matter subhaloes (Carlberg et al. 2012; Sanders et al. 2016; Erkal et al. 2017; Bonaca et al. 2019; Banik & Bovy 2019; Bonaca et al. 2020).

The first detections of streams included the discovery of the tidally distorted Sagittarius Dwarf Galaxy by Ibata et al. (1994), the tidal tails around multiple globular clusters by Grillmair et al. (1995) and the Helmi streams by Helmi et al. (1999). Since then, the number of known streams has grown rapidly owing to the high-quality data from wide-field surveys. The first surge in discoveries came with the arrival of the Sloan Digital Sky Survey, where among others, the GD-1 (Grillmair & Dionatos 2006b), Orphan (Grillmair 2006; Belokurov et al. 2006), Palomar 5 (Odenkirchen et al. 2001) and NGC 5466 streams (Grillmair & Johnson 2006) were found. More discoveries from other surveys, such as PAndAS, Pan-STARRS1 and the Dark Energy Survey, followed

(Martin et al. 2014; Bernard et al. 2014; Koposov et al. 2014; Bernard et al. 2016; Shipp et al. 2018).

Despite the abundance of known streams (see e.g. Newberg & Carlin 2016; Mateu et al. 2018), full six-dimensional phase space maps of stream members, crucial for obtaining accurate constraints on the Galactic potential, have only been made for a few cases. Recently, the second data release of Gaia (Gaia DR2, Gaia Collaboration et al. 2018) expanded our ability to make such maps by several orders of magnitude, by measuring proper motions for more than a billion Milky Way stars. This phenomenal wealth of data has already facilitated the discovery of many new streams (Malhan et al. 2018; Ibata et al. 2019; Meingast et al. 2019) and prompted further investigations of the previously known ones (Price-Whelan & Bonaca 2018; Price-Whelan et al. 2019; Koposov et al. 2019; Koppelman et al. 2019). To gain a full 6D view of more distant streams, Gaia data must be combined with radial-velocity measurements for faint stars from current or future wide-field spectroscopic surveys such as RAVE (Kunder et al. 2017), S^5 (Li et al. 2019), WEAVE (Dalton et al. 2012), 4MOST (de Jong et al. 2019), SDSS-V (Kollmeier et al. 2017) etc.

Perhaps the most intuitive approach for constraining the Galactic potential with stellar streams is the orbit-fitting technique, where orbits integrated in different potentials are compared with the tracks of observed streams (e.g. Koposov et al. 2010; Newberg et al. 2010). However, the oversimplification that streams perfectly follow the original progenitor’s orbit has been shown to lead to systematic biases when used to constrain the Galactic potential (Sanders & Binney 2013a). More realistic stream modelling involves creating either full N-body simulations of disruptions of stellar clusters (the most accurate but also most computationally expensive option) or particle-spray models, where the stream is created by ejecting stars from the Lagrange points of an analytical model of the progenitor at specific times (Bonaca et al. 2014; Küpper et al. 2015; Erkal et al. 2019).

All these methods compare models to observed streams in 6-dimensional phase space, or some subset of measured positions and velocities. It is, however, possible to simplify the behaviour of streams considerably by switching to action-angle coordinates (McMillan & Binney 2008; Sanders & Binney 2013b; Bovy et al. 2016). In this work we follow the action-space clustering method of Sanderson et al. (2015). Actions are integrals of motion that, save for orbital phase, completely define the orbit of a star bound in a static or adiabatically time-evolving potential. Converting the 6-dimensional phase-space position of a star to action space essentially compresses the entire orbit of a star to just three numbers. Stream stars move along similar orbits and thus should cluster tightly in action space. However, since action calculation requires knowledge of the Galactic potential, clustering occurs only if the actions are calculated with the true potential. Therefore, our strategy to find the true Galactic potential is to identify the potential that produces the most clumpy distribution of stars in action space.

The method outlined in Sanderson et al. (2015) quantifies the degree of action space clustering with the Kullback-Leibler divergence, which is used to determine both the best-fit potential and its associated uncertainties. In that work we demonstrated the effectiveness of this procedure by successfully recovering the input parameters of a potential using

mock streams evolved in that potential. Here, we apply the same technique to real stellar streams.

Stellar streams can possess a variety of morphologies: some appear as long narrow arcs, others shells, while still others are fully phase-mixed and no longer easily distinguishable as single structures (Hendel & Johnston 2015; Amorisco 2015). However, even if phase-mixing has induced a lack of apparent spatial features, the fact that these stars still follow similar orbits causes them to condense into a single cluster in action-space. Our method is thus applicable to streams in any evolutionary stage.

Another important advantage of this technique is that it can be applied to multiple streams simultaneously. Combining multiple streams is crucial since it helps counteract the biases to which single-stream fits have been shown to be susceptible (Bonaca et al. 2014). Single-stream fits that account for only statistical uncertainties are severely limited by systematics, both in the insufficiency of the potential model (compare for example the Law & Majewski (2010) and Vera-Ciro & Helmi (2013) fits to the Sagittarius stream in the era before Gaia) and in the limited range of orbits explored. Only *simultaneous* fitting of multiple streams can begin to probe the extent and nature of these systematic uncertainties by consolidating several independent measurements of the mass profile over a range of Galactic distances.

This paper is organised as follows. In Section 2, we explain the theoretical background and the details of our procedure. In particular, the Stäckel potential used to model the Milky Way is introduced in Section 2.1, the calculation of actions from the observed phase space is described in Section 2.2, and Sections 2.3 and 2.4 discuss how we determine the best-fit potential (see also Appendix B) and confidence intervals, respectively. In Section 3, we introduce the four streams in our sample, giving a brief overview of their properties and an outline of our data sets (for more detail see Appendix A). Our results, for both individual and combined streams, are presented in Section 4 for the one-component model and in Section 5 for the two-component model. Section 6 is dedicated to validating our results and presenting the predicted orbits. In Section 7, we compare our results with other potential models of the Milky Way and discuss the implications, and in Section 8 we summarize our main conclusions.

2 METHOD

To constrain the Milky Way’s gravitational potential, we exploit the idea that stream stars’ action-space distributions bear the memory of their progenitor’s orbit. We describe the Galactic potential with a one- or two-component Stäckel model (§2.1), converting the observed phase space coordinates of each star in our sample into action space coordinates (§2.2) for a wide, *astrophysically motivated* range of Stäckel potential parameters. The model for the potential that produces the most clumped configuration of actions is selected as the best-fit potential (§2.3). Once the best-fit potential is identified, its confidence intervals are determined by quantifying the relative difference between the action distribution in the best-fit potential and those of all other considered potentials (§2.4).

2.1 Stäckel potential

While there exist algorithms to estimate approximate actions for any gravitational potential (see review by [Sanders & Binney 2016](#)), analytical transformation from phase space coordinates to action-angle coordinates is possible only for a small set of potentials. The best suited of these to describe a real galaxy is the axisymmetric Stäckel model ([Batsleer & Dejonghe 1994](#); [de Zeeuw 1985](#)). This work exploits potentials of the Stäckel form, enabling us to explore the relevant parameter space efficiently. In addition, using a potential with analytic actions avoids introducing additional numerical errors from action estimation, which are a function of the actions themselves, and are several orders of magnitude higher for radial than circular orbits ([Vasiliev 2019a](#)).

The Hamilton-Jacobi equation is a formalization of classical mechanics used for solving the equations of motion of mechanical systems (see e.g. [Goldstein 1950](#)). The Stäckel potential, when expressed in ellipsoidal coordinates, allows the Hamilton-Jacobi equation to be solved by the separation of variables and therefore the actions to be calculated analytically. Here, we describe the Stäckel potential using spheroidal coordinates: the limiting case of ellipsoidal coordinates that is used to describe an axisymmetric density distribution.

The transformation from cylindrical coordinates R, z, ϕ to spheroidal coordinates λ, ν, ϕ is achieved using the equation

$$\frac{R^2}{\tau - a^2} + \frac{z^2}{\tau - c^2} = 1, \quad (1)$$

where $\tau = \lambda, \nu$. Hence, this is a quadratic equation for τ with roots λ and ν . The shape of the coordinate system is determined by a and c , which can be interpreted as the scale lengths on the equatorial and meridional planes, respectively. The scale lengths define the axis ratio, $e \equiv \frac{a}{c}$. An oblate density distribution has $a > c$, while a prolate density distribution has $a < c$. Further details about this coordinate system can be found in [de Zeeuw \(1985\)](#) and [Dejonghe & de Zeeuw \(1988\)](#). The Stäckel potential, V , in spheroidal coordinates has the form

$$V(\lambda, \nu) = -\frac{f(\lambda) - f(\nu)}{\lambda - \nu}, \quad (2)$$

$$f(\tau) = (\tau - c^2)\mathcal{G}(\tau),$$

where $\mathcal{G}(\tau)$ is the potential in the $z = 0$ plane, defined as

$$\mathcal{G}(\tau) = \frac{GM_{\text{tot}}}{\sqrt{\tau + c}}, \quad (3)$$

with M_{tot} the total mass and G the gravitational constant. Putting these elements together, we get

$$V(\lambda, \nu) = -\frac{GM_{\text{tot}}}{\sqrt{\lambda + \sqrt{\nu}}}. \quad (4)$$

It is possible to combine two Stäckel potentials for a more realistic model of the Galaxy ([Batsleer & Dejonghe 1994](#)). In this case, we have two components in the full potential, V_{outer} and V_{inner} , each following Equation 2. In [Batsleer & Dejonghe \(1994\)](#) the inner component is intended to represent the disc, while the outer component is associated with the halo. However, for our work the individual components are not intended to represent specific structures of the Milky Way; their purpose is simply to add more flexibility

to our model. The two components have different axis ratios and scale radii, which indicates that we are dealing with two separate coordinate systems, one defined by parameters $a_{\text{outer}}, c_{\text{outer}}$ and the other by parameters $a_{\text{inner}}, c_{\text{inner}}$, in which the Hamilton-Jacobi equation is separable for each of the two components. For the overall potential to retain the Stäckel form (as defined by Equation 2), and hence the separability of the Hamilton-Jacobi equation, the two sets of spheroidal coordinates must be related by

$$\lambda_{\text{outer}} - \lambda_{\text{inner}} = \nu_{\text{outer}} - \nu_{\text{inner}} = q, \quad (5)$$

and the parameters of the the two components' coordinate systems have to be linked by

$$a_{\text{outer}}^2 - a_{\text{inner}}^2 = c_{\text{outer}}^2 - c_{\text{inner}}^2 = q, \quad (6)$$

where q is a constant. The total potential is then

$$V(\lambda_{\text{outer}}, \nu_{\text{outer}}, q) = -GM_{\text{tot}} \left[\frac{1 - k}{\sqrt{\lambda_{\text{outer}} + \sqrt{\nu_{\text{outer}}}}} + \frac{k}{\sqrt{\lambda_{\text{outer}} - q + \sqrt{\nu_{\text{outer}} - q}}} \right] \quad (7)$$

where k is the ratio of the inner component mass to the outer component mass, and M_{tot} is the sum of the two component masses. We restrict our model to potentials where the inner component has an oblate shape, i.e. $e_{\text{inner}} > 1$, suitable for the inner regions of the Milky Way. Through the connection between the coordinate systems, this choice forces the outer component also to have $e_{\text{outer}} > 1$, meaning the overall model is limited to quasi-spherical and oblate shapes. In addition, we require the inner component to be flatter than the outer component by restricting $q > 0$.

We first consider a model that consists of a single component represented by a Stäckel potential. The set of three parameters that defines a particular potential is $\theta = (M_{\text{tot}}, a, e)$. We select trial potentials by drawing 40 points from a uniform distribution in log space for each parameter over its prior range: $[0.7, 1.8]$ in $\log_{10}(a/\text{kpc})$, $[11.5, 12.5]$ in $\log_{10}(M/M_{\odot})$, and $[\log_{10}(0.5), \log_{10}(2.0)]$ in $\log_{10}(e)$. Consequently, there are 40^3 trial potentials for this model.

Next, we consider two-component Stäckel potential, defined by a set of five parameters $\theta = (M_{\text{tot}}, a_{\text{outer}}, e_{\text{outer}}, a_{\text{inner}}, k)$. In this case the parameters are not all independent, but are constrained by Equations (6). Thus, we select the trial potentials by drawing 50 points for the shape parameters, again from uniform distributions in log space, over the following ranges: $[0.7, 1.8]$ in $\log_{10}(a_{\text{outer}}/\text{kpc})$, $[\log_{10}(1.0), \log_{10}(2.0)]$ in $\log_{10}(e_{\text{outer}})$ and $[\log_{10}(0.5), \log_{10}(0.7)]$ in $\log_{10}(a_{\text{inner}})$. Of these, we only use the (~ 8000) parameter combinations that allow us to construct a mathematically valid potential; i.e., one where both e_{inner} and e_{outer} are larger than 1. In addition, we draw 20 points for the mass parameters in these parameter ranges: $[11.5, 12.5]$ in $\log_{10}(M/M_{\odot})$ and $[\log_{10}(0.01), \log_{10}(0.3)]$ in $\log_{10}(k)$. For each of these potentials we find the mass enclosed within $r = R^2 + z^2$ by calculating

$$M(< r) = 2\pi \int_0^r \int_{-\sqrt{r^2 - R^2}}^{\sqrt{r^2 - R^2}} \rho(R, z) R dz dR, \quad (8)$$

where the density $\rho(R, z)$ is found through the Poisson equation. Therefore, rather than determining the mass enclosed within an isodensity contour, we integrate the density profile out to a spherical r in order to compare with previous work.

2.2 Actions

In this work, we analyse stellar data in action-angle coordinates. The actions are integrals of motion that uniquely define a bound stellar orbit and the angles are periodic coordinates that define the phase of the orbit. For a bound, regular orbit¹, the actions J_i are related to the coordinates q_i and their conjugate momenta p_i by

$$J_i = \frac{1}{2\pi} \oint p_i dq_i, \quad (9)$$

where the integration is over one full oscillation in q_i . In the spheroidal coordinate system defined in §2.1, $q_1 = \lambda$, $q_2 = \nu$ and $q_3 = \phi$. The expressions for the actions in the Stäckel potential are found by solving the Hamilton-Jacobi equation via separation of variables (see e.g. Binney & Tremaine 2008). This leads to the definition of three integrals of motion: the total energy E , and the actions I_2 and I_3 ; and to the equations for the momenta. The integral of motion I_2 is related to the angular momentum in the z-direction,

$$I_2 = \frac{L_z^2}{2}, \quad (10)$$

while I_3 can be seen as a generalization of $L - L_z$ (Dejonghe & de Zeeuw 1988),

$$I_3 = \frac{1}{2}(L_x^2 + L_y^2) + (a^2 - c^2) \left[\frac{1}{2}v_z^2 - z^2 \frac{G(\lambda) - G(\nu)}{\lambda - \nu} \right]. \quad (11)$$

The momenta, p_τ , are then expressed as a function of the τ coordinate and the three integrals of motion:

$$p_\tau^2 = \frac{1}{2(\tau - a^2)} \left[G(\tau) - \frac{I_2}{\tau - a^2} - \frac{I_3}{\tau - c^2} + E \right], \quad (12)$$

from which the first two actions can be calculated as

$$J_\tau = \frac{1}{2\pi} \oint p_\tau d\tau, \quad (13)$$

where the integral is over the full oscillation of the orbit in τ , i.e. the limits are the roots of p_τ^2 . As p_τ is only a function of τ and the three integrals of motion, it follows that J_τ is also an integral of motion. The third action, J_ϕ , is equal to L_z and therefore independent of the particular axisymmetric potential.

We calculate the actions for all stars in our sample for each trial potential. From the observed sky positions and proper motions in Gaia DR2, cross-matched with distance and radial velocity estimators from the various sources discussed in §3, we derive the Galactocentric phase-space coordinates $\omega = (\mathbf{x}, \mathbf{v})$, where \mathbf{x} is the three-dimensional position vector and \mathbf{v} is the three-dimensional velocity vector. Details of this transformation are given in Appendix A. The phase-space coordinates are then used to calculate (τ, p_τ) and E , I_2 and I_3 for each star in each trial potential. As mentioned before, $J_\phi = L_z$ and does not vary from potential to potential. The other two actions, J_λ and J_ν , are found from Equation 13 by numerical integration. We discuss the influence of measurement errors in §6.

Some combinations of observed phase-space coordinates and trial potential can result in the star being unbound from

the Galaxy, in which case its actions are undefined. In our analysis, we throw out any potential that produces unbound stars, a reasonable assumption given that the stars in our data set are all well within the Galaxy's expected virial radius and have velocities much less than estimates of the escape velocity. We comment on the impact of this choice on our results in §6.

2.3 Determination of the best-fit potential

In the previous section, we transformed the phase space coordinates of stream stars to action space coordinates for particular trial potentials. Now, we analyse the resulting action distributions to measure their degree of clustering. We quantify the degree of clustering with the use of the Kullback-Leibler divergence following Sanderson et al. (2015). The Kullback-Leibler divergence (KLD) measures the difference between two probability distributions $p(\mathbf{x})$ and $q(\mathbf{x})$ and is defined by

$$\text{KLD}(p \parallel q) = \int p(\mathbf{x}) \log \frac{p(\mathbf{x})}{q(\mathbf{x})} d^n x. \quad (14)$$

The larger the difference between the two probability distributions, the larger the value of the associated KLD. If the two distributions are identical the KLD value is 0.

For a discrete sample $[\mathbf{x}_i]$ with $i = 1, \dots, N$ drawn from a distribution $p(\mathbf{x})$, the KLD can be calculated via Monte Carlo integration as

$$\text{KLD}(p \parallel q) \approx \frac{1}{N} \sum_i^N \log \frac{p(\mathbf{x}_i)}{q(\mathbf{x}_i)}, \quad \text{if } q(\mathbf{x}_i) \neq 0 \ \forall i. \quad (15)$$

We now specify the distribution $q(\mathbf{x})$ to be a uniform distribution $u(\mathbf{J})$, in the actions. This uniform distribution corresponds to a fully unclustered action space. To test whether a trial potential parameterized by $\boldsymbol{\theta}$ maps the observed phase space data ω to a more clustered distribution than $u(\mathbf{J})$, we set $p(\mathbf{x})$ to $p(\mathbf{J} \mid \boldsymbol{\theta}, \omega)$. $p(\mathbf{J} \mid \boldsymbol{\theta}, \omega)$ is the probability distribution p of actions \mathbf{J} , given parameter values $\boldsymbol{\theta}$ and the phase space coordinates ω .

The Kullback-Leibler divergence is then

$$\text{KLD1}(\boldsymbol{\theta}) = \frac{1}{N} \sum_i^N \log \frac{p(\mathbf{J} \mid \boldsymbol{\theta}, \omega)}{u(\mathbf{J})} \Big|_{\mathbf{J}=\mathbf{J}_\theta^i}, \quad (16)$$

where N is the total number of stars in our sample. p is evaluated at $\mathbf{J}_\theta^i = \mathbf{J}(\boldsymbol{\theta}, \omega_i)$, where ω_i are the phase space coordinates of star i . The potential closest to the true potential gives rise to the most clumped probability distribution; i.e., the distribution that is the most peaked and therefore most *dissimilar* to a uniform distribution. We therefore select as our best-fit potential, $\boldsymbol{\theta}_0$, the one that maximises the Kullback-Leibler divergence across all our trial potentials. This is equivalent to selecting the model that produces the most similar orbits for all stars in a given stream, by exploring all possible star orbits over a range of models given their current phase space coordinates. We label Equation 16 as KLD1 because the identification of the best-fit model is the first step in our procedure. Practically, we calculate KLD1 using Equation 16 for all potentials that are not discarded for producing unbound stars. We obtain the numerator in Equation 16 by constructing a three-dimensional probability density function $p(\mathbf{J} \mid \boldsymbol{\theta}, \omega)$ using the entropy-based space

¹ An orbit for which the angle-action variables exist (Binney & Tremaine 2008).

partitioning algorithm Enlink developed by [Sharma & Johnston \(2009\)](#).

The denominator in Equation 16, $u(\mathbf{J})$, is a uniform distribution normalised over the maximum possible range of \mathbf{J} :

$$u = \left[(J_\lambda^{\max} - J_\lambda^{\min}) (J_\nu^{\max} - J_\nu^{\min}) (J_\phi^{\max} - J_\phi^{\min}) \right]^{-1}, \quad (17)$$

where \mathbf{J}^{\max} and \mathbf{J}^{\min} are the extrema amongst all \mathbf{J} calculated for our five-parameter search. This means $u(\mathbf{J})$ is constant for all \mathbf{J} and all $\boldsymbol{\theta}$ and as such does not have an impact on maximizing KLD1($\boldsymbol{\theta}$).

The *standard* KLD1($\boldsymbol{\theta}$), calculated using Equation 16, gives equal weight to each of the stars in the sample, and it is suited to cases where our data sample includes either a single stream or multiple streams with unknown stellar membership. However when combined stellar stream data are analysed and star membership *is* known, as it is in our case, we can exploit this extra information and modify Equation 16 accordingly. Equation 16 has the implicit property that streams with more stars exert a larger influence on the results compared to streams with fewer stars, since each star contributes equally to the KLD. While this is reasonable when membership is not known a priori, it is not the ideal use of the data since then the largest and hottest streams, which give the least sensitive constraints, dominate over thinner and colder streams with far fewer members. When membership information is available, we can instead introduce a scheme that gives equal weight to all *streams*, by weighting the contribution of each star with:

$$w_j = \frac{1}{N_s} \times \frac{1}{N_j}, \quad (18)$$

where N_s is the number of streams in our sample and N_j is the number of stars in stream “ j ” (and therefore $N = \sum_j^{N_s} N_j$). This *weighted* KLD1($\boldsymbol{\theta}$) is thus calculated as follows:

$$\text{wKLD1}(\boldsymbol{\theta}) = \sum_j^{N_s} \sum_i^{N_j} w_j \log \frac{p(\mathbf{J} \mid \boldsymbol{\theta}, \boldsymbol{\omega})}{u(\mathbf{J})} \Big|_{\mathbf{J}=\mathbf{J}_\theta^{i_j}} \quad (19)$$

where $\mathbf{J}_\theta^{ij} = \mathbf{J}(\boldsymbol{\theta}, \boldsymbol{\omega}_{ij})$, where $\boldsymbol{\omega}_{ij}$ are the phase space coordinates for star i in stream j .

The KLD works best if there is little overlap between the different streams in action-space. We showed in previous work ([Sanderson et al. 2015](#)) that the clustering-maximization algorithm will still find a good model potential if the streams overlap, and does not crucially depend on knowing stream membership. However, in our case, stream membership is known, and the performance of the algorithm can be further improved by incorporating this information in the *weighted* KLD1 approach. The most straightforward way of doing this is simply to shift each stream by a constant in action space so that they are well-separated, since it is the *clustering*, not the *location* in action space, that drives the fit.² This tactic also helps avoid the spurious solution achieved by increasing the mass and decreasing the

² In fact, in previous papers we used the product of the marginal distributions of p instead of the uniform distribution as the comparison distribution q ; this form of the KLD is known as the mutual information (MI), and for a multivariate Gaussian it can be shown that the MI depends only on the off-diagonal elements

scale radius until all stars are clustered near the origin in action space, which sometimes can dominate over the true consensus fit for severely overlapping streams or in cases with a high fraction of interlopers from the thick disc. For this work we displace the streams from one another in L_z , since this action is independent of the potential for our axisymmetric model. On the other hand, when performing our analysis with the standard KLD1 (Equation 16) this shift in action space will *not* be applied.

2.4 Determination of confidence intervals

One interpretation of the KLD is that of an average log-likelihood ratio of a data set. The likelihood ratio,

$$\Lambda = \prod_i^N \frac{p(\mathbf{x}_i \mid \boldsymbol{\theta})}{q(\mathbf{x}_i \mid \boldsymbol{\theta})}, \quad (20)$$

indicates how much more likely \mathbf{x} is to occur under $p(\mathbf{x} \mid \boldsymbol{\theta})$ than under $q(\mathbf{x} \mid \boldsymbol{\theta})$, where we recall that $p(\mathbf{x} \mid \boldsymbol{\theta})$ and $q(\mathbf{x} \mid \boldsymbol{\theta})$ are probability density functions. Therefore, the average log-likelihood ratio for x_i is

$$\langle \log \Lambda \rangle = \frac{1}{N} \sum_i^N \log \frac{p(\mathbf{x}_i \mid \boldsymbol{\theta})}{q(\mathbf{x}_i \mid \boldsymbol{\theta})}, \quad (21)$$

which is equivalent to calculating the Kullback-Leibler divergence. The interpretation of KLD as an average log-likelihood ratio allows us to draw confidence intervals on the best-fit parameters through Bayes’ theorem, which states that the posterior probability of a model defined by its parameters $\boldsymbol{\theta}$, given data \mathbf{x} , is equal to the likelihood of the data given the model times the prior probability of the model:

$$p(\boldsymbol{\theta} \mid \mathbf{x}) \propto p(\mathbf{x} \mid \boldsymbol{\theta})p(\boldsymbol{\theta}). \quad (22)$$

This indicates that the ratio of likelihoods is directly linked to the ratio of posterior probabilities:

$$\begin{aligned} \text{KLD}(p \parallel q) &= \frac{1}{N} \sum_i^N \log \frac{p(\mathbf{x}_i \mid \boldsymbol{\theta})}{q(\mathbf{x}_i \mid \boldsymbol{\theta})} \\ &= \frac{1}{N} \sum_i^N \log \frac{p(\boldsymbol{\theta} \mid \mathbf{x}_i)}{q(\boldsymbol{\theta} \mid \mathbf{x}_i)} - \log \frac{p(\boldsymbol{\theta})}{q(\boldsymbol{\theta})} \end{aligned} \quad (23)$$

Assuming that the prior distributions are flat or equal, the KLD is thus equal to the expectation value of the log of the ratio of posterior probabilities (for more information, see [Kullback 1959](#)).

This leads us to the second step in our procedure, where we compare the action distribution of the best-fit potential, $p(\mathbf{J} \mid \boldsymbol{\theta}_0, \boldsymbol{\omega})$, to the action distributions of the other trial potentials, $p(\mathbf{J} \mid \boldsymbol{\theta}_{\text{trial}}, \boldsymbol{\omega})$, by computing

$$\text{KLD2}(\boldsymbol{\theta}) = \frac{1}{N} \sum_i^N \log \frac{p(\mathbf{J} \mid \boldsymbol{\theta}_0, \boldsymbol{\omega})}{p(\mathbf{J} \mid \boldsymbol{\theta}_{\text{trial}}, \boldsymbol{\omega})} \Big|_{\mathbf{J}=\mathbf{J}_0^i}, \quad (24)$$

where both functions are evaluated at $\mathbf{J}_0 = \mathbf{J}(\boldsymbol{\theta}_0, \boldsymbol{\omega})$, i.e. at the actions computed with the best-fit potential $\boldsymbol{\theta}_0$ and

of the covariance matrix – or in other words, on the correlation between actions.

phase space ω . In our procedure, we use equation 24 to calculate the $\text{KLD2}(\theta)$ for each trial potential. In contrast to the calculation of the $\text{KLD1}(\theta)$, two different sets of actions are used to obtain the probability density functions in the numerator and the denominator: both sets of actions are calculated using the same observed phase space coordinates ω but two different potentials (the best-fit potential θ_0 and another trial potential θ_{trial}). We use Enlink to estimate the probability densities for the two sets of actions $\mathbf{J}(\theta_0, \omega)$ and $\mathbf{J}(\theta_{\text{trial}}, \omega)$.

Analogous to $\text{KLD1}(\theta)$, we introduce an alternative version of $\text{KLD2}(\theta)$ that incorporates weights. The weighted $\text{KLD2}(\theta)$ is defined as follows:

$$\text{wKLD2}(\theta) = \sum_i^N w_i \log \frac{p(\mathbf{J} \mid \theta_0, \omega)}{p(\mathbf{J} \mid \theta_{\text{trial}}, \omega)} \Big|_{\mathbf{J}=\mathbf{J}_0^i}. \quad (25)$$

where the weights are calculated using Equation 18.

As discussed above, the $\text{KLD2}(\theta)$ values can be interpreted as the relative probability of parameters θ_0 and θ_{trial} , given the data. The confidence intervals on the best-fit potential are then derived by estimating the value of $\text{KLD2}(\theta)$ at which the posterior distributions become significantly different, i.e. $\text{KLD2}(\theta)$ becomes significantly different from $\text{KLD2}(\theta_0) = 0$.

We begin by assuming that the probability distributions for the single-component (three-parameter) model are approximately three-dimensional Gaussians with a covariance matrix Σ that is equal to a 3×3 identity matrix. We calculate $\text{KLD2}(\theta)$ between two of these identical Gaussian distributions placed at different positions: one centred at θ_0 representing the probability distribution of our best-fit model and the other centred at θ_{trial} representing the probability distribution of a trial model. Since we are interested in determining which of our trial models are within 1σ of our best-fit model, we use here the limiting case for θ_{trial} , that is the case where the Gaussian for the trial model is centred at exactly 1σ away from θ_0 in all three dimensions. Calculation of the $\text{KLD2}(\theta)$ between these two distributions results in a $\text{KLD2}(\theta)$ value that corresponds to a 1σ confidence interval in three dimensions. Similarly, the $\text{KLD2}(\theta)$ value that signifies the limiting edge of 2σ confidence can be calculated using a trial model that is centred at exactly 2σ away from θ_0 in all three dimensions, etc. The single parameter 1σ confidence intervals are drawn as the full range of parameter values in the subset of potentials that are within 1σ from the best-fit potential.

Similar reasoning allows us to draw confidence intervals also on the best-fit parameters of the two-component (five-parameter) potential. This time, we assume that the probability distributions are five-dimensional Gaussians and that the Gaussian for the trial model is centred at 1σ away from θ_0 in all five dimensions. The resulting KLD2 values for 1 , 2 and 3σ , for both single- and two-parameter models, are given in Table 1.

3 STREAM CATALOGUE

The goal of this work is to use the action space clustering method on real data of known stream stars. For this purpose we compiled data from 7 different literature sources

	1σ	2σ	3σ
KLD2	1.5	6	13.5
KLD2	2.5	10	22.5

Table 1. KLD2 values corresponding to 1, 2 and 3σ confidence intervals: *upper* line: single-component case; *lower* line: two-component case.

(Koposov et al. 2010; Willett et al. 2009; Li et al. 2017; Koposov et al. 2019; Price-Whelan et al. 2019; Ibata et al. 2017; Koppelman et al. 2019) to obtain a data set containing full 6D phase-space information for stars in the GD-1, Helmi, Orphan and Palomar 5 streams. When complete 6D information for individual stars was not available, we made use of the stream’s track: the measurements of the stream’s mean phase-space position as a function of a coordinate aligned with the stream. We fit the tracks with a simple polynomial function in order to find the stars’ missing 6D phase space components, based on their location along the stream. We do not assign membership probabilities to the stars in each stream, but rather treat all of them as certain members. A perfectly clean selection of stream stars is not crucial for our method, which can operate without any membership information at all since it relies on finding the most clustered *total* action distribution. The addition of stars incorrectly classified as stream members—as long as such stars are in the minority—will simply result in slightly less clustered action-space for each of the trial potentials. We do not expect interlopers to bias the result: since stream membership is usually determined by making selections in some combination of positions, velocities, colors and magnitudes rather than in actions, it is unlikely that interlopers will cluster with the rest of the stream in action space near the best-fit potential.

Nevertheless, to focus on the most informative stars, we perform cuts on some of the streams after visually inspecting them in $\mu_\alpha - \mu_\delta$ or $L_z - L_\perp$ space (we discuss the possible impact of this cut in section 6). Our full data set is available in electronic format online. In the following, we briefly review each stream’s properties and compiled data set. For more details on our data assembly process we refer to Appendices A1-A3.

3.1 The GD-1 stream

GD-1 is a long and remarkably narrow stream first discovered by Grillmair & Dionatos (2006b) in the SDSS data. It lies at a distance of ~ 15 kpc from the Galactic center and ~ 8 kpc above the plane of the disc. Due to its thinness and location high above the Galactic disc it is thought to have formed from a tidally disrupted globular cluster, but no progenitor has yet been found. Orbits fitted to the available data have shown that GD-1 is moving retrograde with respect to the rotation of the Galactic disc, and is currently near pericentre (around 14 kpc), with apocentre 26–28 kpc from the Galactic centre (Willett et al. 2009; Koposov et al. 2010).

The GD-1 stream has seen considerable use in studies aiming to constrain the inner Galactic potential. For example, using a single component potential Koposov et al. (2010) find that the orbit that best fits the GD-1 data corresponds to a potential with the circular velocity at the

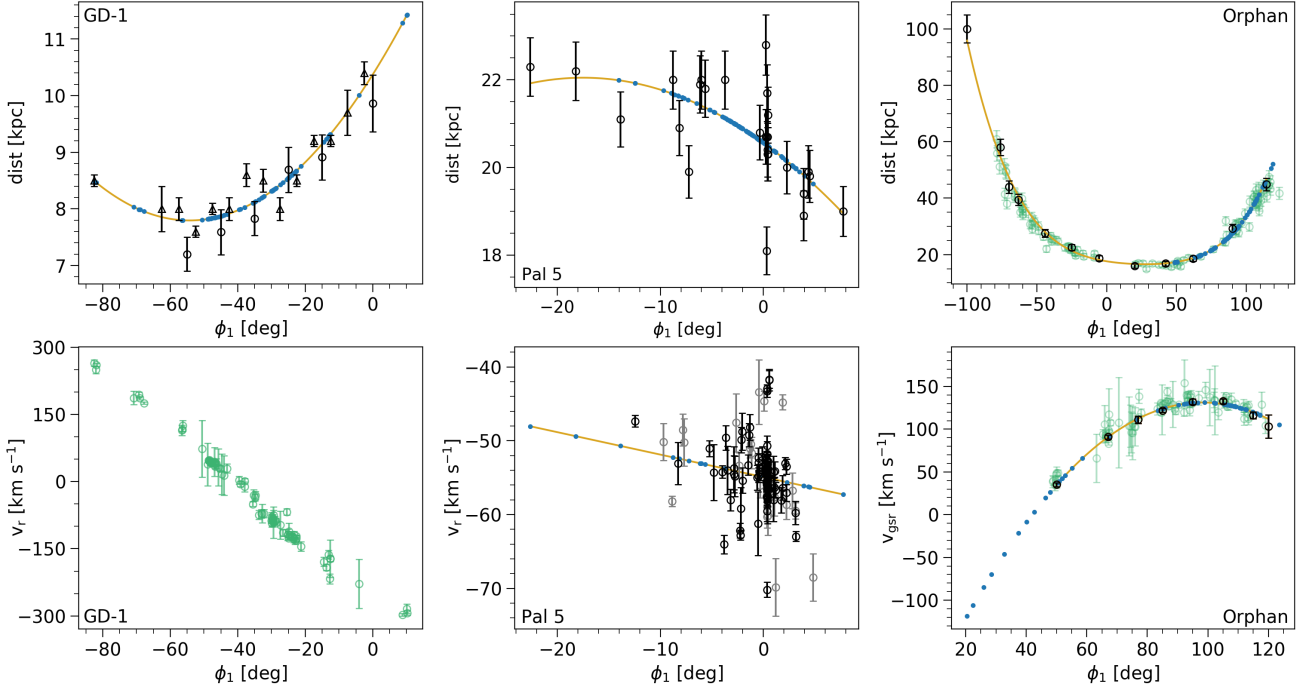


Figure 1. Fits used to interpolate missing distance and radial velocity (RV) data for stream stars. The coordinate ϕ_1 on the x-axis is the stream-aligned coordinate for the stream portrayed on each particular panel. Measurements used for the polynomial fits are shown in black (> 0.5 membership probability) or gray points (< 0.5 membership probability); measurements for individual stars shown as green points are for comparison only. Polynomial fits are shown in yellow; estimated values we adopt for individual stars are shown as small blue points. Data sources are discussed in detail in Appendix A. **Top left:** fit to distance estimates along the track of GD-1 from Koposov et al. (2010) (circles) and Li et al. (2018) (triangles). **Bottom left:** RV measurements from Koposov et al. (2010), Li et al. (2017) and Willett et al. (2009). **Top centre:** fit to distances of individual Pal 5 members from Price-Whelan et al. (2019). **Bottom centre:** fit to RVs of individual Pal 5 members from Ibata et al. (2017). **Top right:** fit to distance estimates along the track of the Orphan Stream from Koposov et al. (2019) Individual measurements from Koposov et al. (2019) (green points) are shown for comparison. **Bottom right:** fit to RV estimates along the track of the Orphan stream from Koposov et al. (2019) (in the Galactic standard of rest frame). Individual measurements from Li et al. (2017) (green points) are shown for comparison.

solar radius $V_c(R_\odot) = 221^{+16}_{-20} \text{ km s}^{-1}$ and the flattening $q = 0.87^{+0.12}_{-0.03}$. A more recent work by Malhan & Ibata (2019), which uses a combination of Gaia DR2, SEGUE and LAMOST data, finds a circular velocity at the solar radius of $V_c(R_\odot) = 244 \pm 4 \text{ km s}^{-1}$, the flattening of the halo $q = 0.82^{+0.25}_{-0.13}$ and the mass enclosed within 20 kpc $M(< 20 \text{ kpc}) = 2.5 \pm 0.2 \times 10^{11} M_\odot$.

We compiled a list of GD-1 members with measured radial velocities from Koposov et al. (2010), Li et al. (2017) and Willett et al. (2009). These stars' measurements are then supplemented with positions and proper motions from Gaia DR2. Finally, we fit a polynomial to the stream track distance information from Koposov et al. (2010) and Li et al. (2018) and use the resulting function to predict distances to each of our stream members based on their location along the stream. In total our GD-1 data set consists of 82 member stars with full 6D phase space information. We further clean this sample by discarding 13 stars that are not part of the central clump in either $\mu_\alpha - \mu_\delta$ or $L_z - L_\perp$ space, leaving 69 stars (see Appendix A1).

3.2 Orphan Stream

The Orphan stream was discovered by Grillmair (2006) and Belokurov et al. (2006) as a broad stream of stars extending

~ 60 degrees in the Northern Galactic hemisphere. Although thought to be the remnant of a small dwarf galaxy (Grillmair 2006), no suitable progenitor for the stream has so far been found. Using SDSS DR7 data, Newberg et al. (2010) obtained a well-defined orbit to the stream and showed that the stars are on a prograde orbit with respect to disc rotation with a pericentre of 16 kpc and an apocentre of 90 kpc. At the time, the detected portion of the stream ranged from ~ 20 to ~ 50 kpc in the Galactic frame.

Recently, several discoveries regarding the Orphan stream were made by Koposov et al. (2019) who traced the track of the Orphan stream using RR Lyrae in the Gaia DR2 catalogue. They found that the stream is much longer than previously thought and showed that it also extends to the Southern Galactic hemisphere: the stream was found to extend from ~ 50 kpc in the North to ~ 50 kpc in the South, going through its closest approach at ~ 15 kpc from the Galactic Centre. They noticed, however, that the stream track behaviour changes between the two hemispheres. First, a twist in the stream track emerges soon after the stream crosses the Galactic plane from south to north. Second, the motion of the stars in the southern hemisphere is not aligned with the stream track. Erkal et al. (2019) show that these effects can be reproduced by adding the contribution of the Large Magellanic Cloud (LMC) into the Milky Way poten-

tial. These results demonstrate that the assumption that the Orphan stream stars orbit in a static Milky Way potential would lead to a bias.

Using the Orphan stream RR Lyrae from [Koposov et al. \(2019\)](#) and including the perturbation from the LMC [Erkal et al. \(2019\)](#) find that the best fit Milky Way potential has a mass enclosed within 50 kpc of $3.80_{-0.11}^{+0.14} \times 10^{11} M_{\odot}$ and scale radius of the NFW halo of $17.5_{-1.8}^{+2.2}$ kpc. As a comparison, when using only the Northern portion of the stream [Newberg et al. \(2010\)](#) find that the orbit is best fit to a Milky Way potential which has a mass enclosed within 60 kpc of about $2.6 \times 10^{11} M_{\odot}$.

We assemble our Orphan Stream data in two parts. In both cases the positions and proper motions are from Gaia DR2, but accurate individual distances and radial velocities have been measured for disparate sets of stars.

To compile the first subsample, we begin with a list of stream members that have accurate distance measurements: the Orphan stream RR Lyrae from [Koposov et al. \(2019\)](#). We fit a polynomial to the radial velocity track information from [Koposov et al. \(2019\)](#) and use it to predict radial velocities to our stream members based on their location along the stream. Although the RR Lyrae stars stretch from $\phi_1 \sim -78$ to ~ 123 degrees, we discard those that have $\phi_1 < 0$, i.e. those in the Southern Galactic hemisphere. We do this because there are no radial velocity measurements in the negative ϕ_1 section of the stream (see the bottom right panel of Figure 1), leading our estimates to depend too heavily on the selection of the degree of the polynomial and its fit to the positive ϕ_1 section of the stream. As an added advantage, this cutoff eliminates the part of the stream that appears to be most strongly affected by the LMC, which is not in our potential model.

To compile the second subsample, we begin with a list of stream members that instead have individual radial velocity measurements: the stream members from [Li et al. \(2017\)](#) with radial velocities from SDSS or LAMOST. Next, we fit a polynomial to the distance track data from [Koposov et al. \(2019\)](#) to find distances for the stars.

After combining the two data sets, we make an additional cut in $L_z - L_{\perp}$ and $\mu_{\alpha} - \mu_{\delta}$ space, selecting after visual inspection the 129 stars that form a clump in velocity space. More details can be found in Appendix A2.

3.3 The Palomar 5 stream

The tidal streams around the Palomar 5 globular cluster were first found by [Odenkirchen et al. \(2001\)](#). They detected two symmetrical tails on either side of the cluster, extending in total about 2.6 degrees on the sky. Subsequent data has allowed the stream to be traced further out and revealed that the two tidal tails are far from symmetric, the tails having distinctly different lengths and star counts. The current known length of the trailing trail is 23 degrees ([Carlberg et al. 2012](#)) while that of the leading tail is only 3.5 degrees ([Odenkirchen et al. 2003](#)). The reason for the asymmetry is not clear but possible options include perturbations from spiral arms, rotating bar, molecular clouds and dark matter subhaloes ([Pearson et al. 2017; Amorisco et al. 2016; Erkal et al. 2017](#)). Palomar 5 is currently near the apocentre of its prograde orbit, which ranges from pericentre at 7 – 8

kpc to apocentre at around 19 kpc from the Galactic Centre ([Odenkirchen et al. 2003; Grillmair & Dionatos 2006a; Küpper et al. 2015](#)). The stream has previously been used to constrain the Milky Way potential by [Küpper et al. \(2015\)](#) who found the mass enclosed within Palomar 5 apocentre distance to be $M(< 19) \text{ kpc} = (2.1 \pm 0.4) \times 10^{11} M_{\odot}$ and the halo flattening in the z-direction to be $q_z = 0.95_{-0.12}^{+0.16}$.

As before, we use a combination of sources to get full 6D phase space information for stars in the Palomar 5 stream. We use a list of 27 RR Lyrae member stars with distance estimates from [Price-Whelan et al. \(2019\)](#) and another 154 members with radial velocity measurements from [Ibata et al. \(2017\)](#). To find the distances for the members from [Ibata et al. \(2017\)](#) and radial velocities for members from [Price-Whelan et al. \(2019\)](#), we use the measurements of the individual members in the other set, using the same track-fitting strategy as for the other streams. In other words, we fit a polynomial to the distances from [Price-Whelan et al. \(2019\)](#) to find distance estimates for the [Ibata et al. \(2017\)](#) members and, similarly, fit a polynomial to the radial velocity data from [Ibata et al. \(2017\)](#) to find radial velocity estimates for the [Price-Whelan et al. \(2019\)](#) members. As always, the positions and proper motions are from Gaia DR2.

After the two data sets are then joined, a cut in $L_z - L_{\perp}$ and $\mu_{\alpha} - \mu_{\delta}$ space is performed, resulting in the sample of 136 stars. More details can be found in Appendix A3.

Note that since we have adopted the distances from [Price-Whelan et al. \(2019\)](#), our Pal 5 stars are closer than previously reported. [Price-Whelan et al. \(2019\)](#) find a mean cluster heliocentric distance of 20.6 ± 0.2 kpc while previous distance measurements are ~ 23 kpc [e.g.] ([Odenkirchen et al. 2001; Carlberg et al. 2012; Erkal et al. 2017](#)). The main cause for this distinction is that the previously reported distances were computed from distance moduli ([Harris 1996; Dotter et al. 2011](#)) that were not corrected for dust extinction.

3.4 The Helmi stream

The Helmi stream was first detected by [Helmi et al. \(1999\)](#) as a cluster of 12 stars in the angular momentum space of the local halo, based on Hipparcos measurements. The orbit of the stream was found to be confined within 7 and 16 kpc from the Galactic Centre. While forming a single clump in $L_z - L_{\perp}$ diagram, in velocity space the structure separates into two distinct groups: one with positive v_z and the other with negative v_z . [Helmi et al. \(1999\)](#) postulated that the two clumps originate from a common dwarf galaxy that has since its disruption reached a highly phase-mixed state. This view explains the observed bimodality of v_z as a feature that arises due to the existence of several wraps of the stream near the Solar neighbourhood (as shown in Figure 5 of [Helmi 2008](#); see also [McMillan & Binney 2008](#) for further discussion of this phenomenon).

Using Gaia DR2 data complemented by radial velocities from the APOGEE, RAVE and LAMOST surveys, [Koppelman et al. \(2019\)](#) found 523 new members of the Helmi stream within 5 kpc of the Sun selected in $L_z - L_{\perp}$ space. In this work we include 401 high confidence members that are within 1 standard deviation of the mean radial velocity from the [Koppelman et al. \(2019\)](#) sample with their full 6D phase space information.

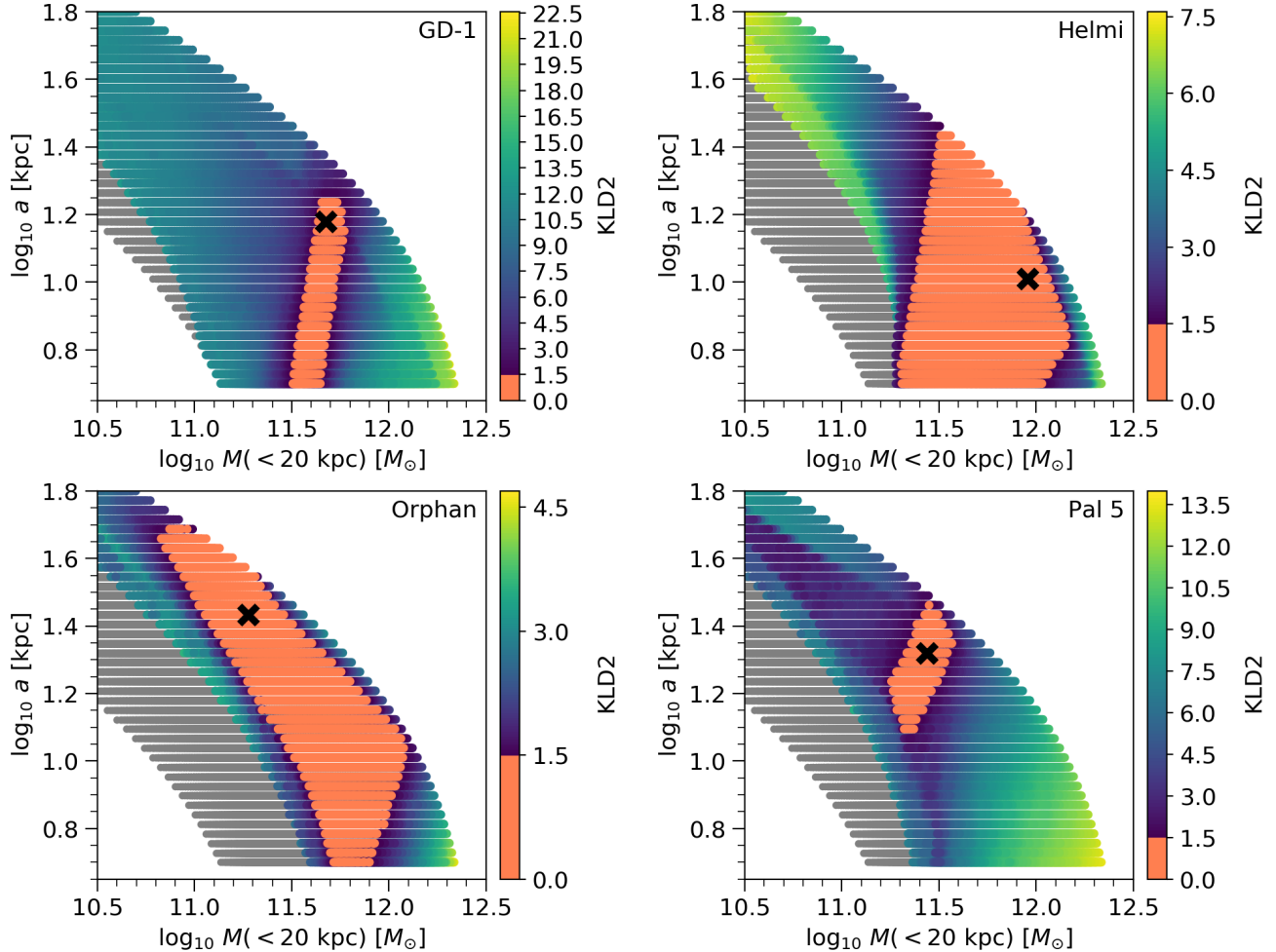


Figure 2. Individual stream results for the single-component potential in the enclosed mass–scale length space. The best-fit point is marked with a black-cross, the grey points represent potentials that resulted in unbound stars and were therefore discarded, and other points are colour-coded according to their KLD2 value. The orange region shows 1σ contours (defined as described in §2.4).

4 RESULTS FOR A SINGLE-COMPONENT POTENTIAL

In this section we present our results for a single-component Stäckel potential with both individual and combined stream data sets (Sec. 4.1 and Sec. 4.2, respectively). The best-fit parameter values (those that maximize KLD1) and uncertainties (derived from KLD2) are summarised in Table 2. Here, we focus on the KLD2 distributions, while those for KLD1 can be found in Appendix B. The KLD1 values associated with the best-fit parameters are given in Table B1, and Figure B1 gives an example of a KLD1 distribution, alongside the action distributions produced by two different potentials.

4.1 Results for the individual stream data sets

Figure 2 shows the individual results for GD-1, Helmi, Orphan and Pal 5 on the enclosed mass – scale length plane. The parameter space is colour-coded by their KLD2 values. The smaller the KLD2 value, the more similar the action distribution of that potential is to the action distribution of the best-fit potential. The potentials with values of $\text{KLD2} \leq 1.5$

- marked in Figure 2 with orange - is the 1σ region, as explained in Section 2.3. The grey points stand for discarded potentials, where at least one star is on a dynamically unbound orbit as discussed in Section 2.2.

Figure 2 indicates that the GD-1 and Pal 5 streams deliver constraints that are much more precise than the Orphan and Helmi streams. Specifically, although Orphan and Helmi streams discard a large section of the parameter space completely due to the emergence of unbound stars, GD-1 and Palomar 5 are more effective in discriminating between potentials that produce only bound orbits. The best-fit values for $M(< 20 \text{ kpc})$ range from 1.89×10^{11} to $\sim 9 \times 10^{11} M_\odot$ between individual streams, with the Orphan stream returning the lowest and Helmi stream the highest estimates. Although their best-fit values differ by an order of magnitude, the derived confidence intervals are compatible: all four streams accept $M(< 20 \text{ kpc})$ values from $\sim 3.2 \times 10^{11}$ up to $\sim 3.7 \times 10^{11} M_\odot$ within 1σ .

With the exception of Palomar 5, the individual streams cannot place strong constraints on the scale length of the potential: the best-fit values range from 10.24 to 27.12 kpc between individual streams, with the Helmi stream yielding the lowest and the Orphan stream the highest values. All

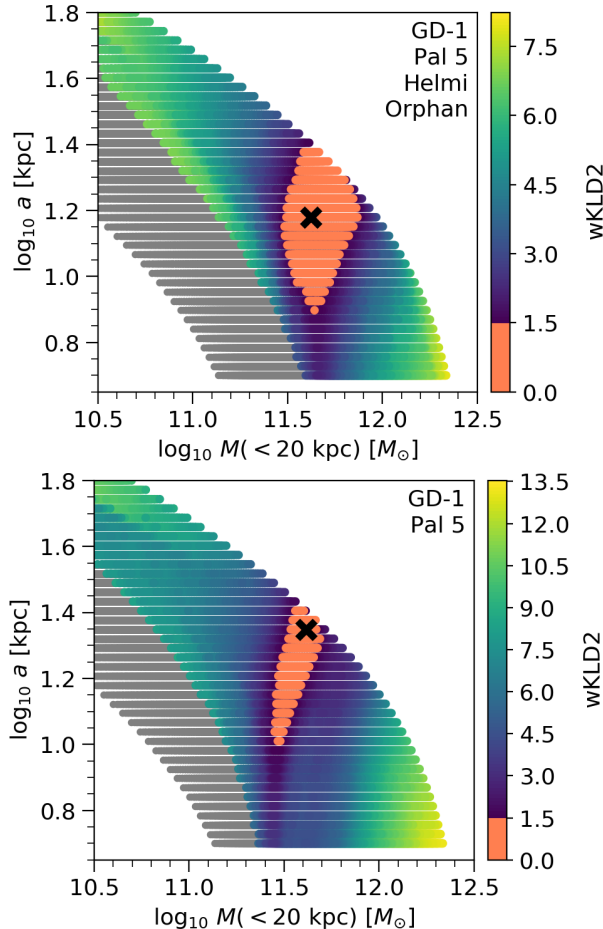


Figure 3. As in Figure 2, but showing the weighted combined data results for the single-component potential. **Top:** results when combining all four streams. **Bottom:** results for the combination of GD-1 and Pal 5 only.

four streams accept a values between ~ 13 kpc and ~ 17 kpc within a 1σ uncertainty level.

The best-fit values for flattening range from 0.88 to 1.40, with the lowest estimate belonging to the GD-1 and the highest to the Pal 5 stream. None of the streams yields an upper limit within the explored range. The GD-1 stream is also unable to determine the lower limit, accepting all values on the defined grid within a 1σ confidence interval. The Helmi stream accepts almost all flattening values except the one corresponding to the most prolate ($e = 0.5$) shape. The Pal 5 and Orphan streams, on the other hand, provide a lower limit to flattening, Orphan allowing only some prolate shapes in addition to the oblate shapes ($e \geq 0.88$) and Pal 5 favouring only oblate shapes ($e \geq 1.09$). All streams accept values ≥ 1.09 within a 1σ uncertainty level.

4.2 Results for the combined data set

The weighted combined data results are shown in Figure 3: the combination of all four streams on the top panel and the combination of GD-1 and Pal 5 on the bottom panel. As a reminder, the weighted results incorporate the knowledge of stream membership by (a) calculating the stream-weighted versions of KLD1 and KLD2 (the latter is marked on the

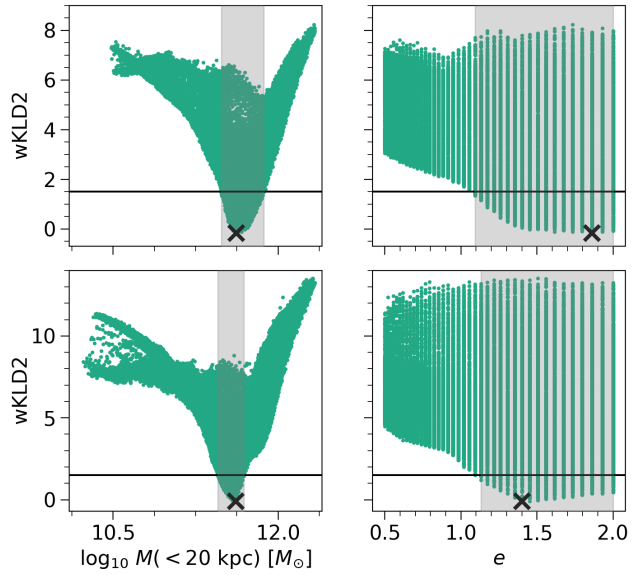


Figure 4. The weighted combined data results for a single-component potential: marginalised single parameter distributions. The top panel shows the results from the combination of all four streams and the bottom panel shows the results of the combination of GD-1 and Pal 5 streams. The green points show the parameter values against the wKLD2 of the potential they belong to. The values of the parameters in the best-fit potentials are marked with a black-cross. The black lines are drawn at wKLD2 = 1.5 which signifies the 1σ confidence interval. The light grey bars show the range of values that are accepted with 1σ confidence.

relevant figures as wKLD2), and (b) by artificially separating streams in action space during the density estimation. This is in contrast to the standard results which assume no knowledge of the stream membership. In this section, we discuss the weighted results only. The standard results will be discussed in the subsequent section.

Constraints from analysing combined data sets are tighter than those yielded by individual stream data sets. Unsurprisingly, the 1σ constraint on the enclosed mass for the combination of GD-1 and Pal 5 data sets is much tighter than that obtained by combining all four streams' data sets. This is an indication that while the limits from GD-1 and Pal 5 are more *precise*, they are not necessarily more *accurate*. The expansion of the confidence interval when the Orphan and Helmi streams are included is confirming that, just as previous work has shown, the different streams have different systematic biases—combining these expands the size of the allowed region. This larger uncertainty from the combination of all four streams is therefore a more robust measure of the actual uncertainties. The two different analyses nonetheless give results that are consistent with each other: we find $4.18^{+3.20}_{-1.14} \times 10^{11} M_\odot$ when analysing the combination of four streams' data and $4.12^{+0.76}_{-1.30} \times 10^{11} M_\odot$ for just the GD-1 and Pal 5 data sets.

Likewise, the scale lengths of the two sets of combined data are in good agreement within the errors: we find $15.12^{+8.70}_{-7.22}$ kpc and $22.32^{+3.10}_{-12.08}$ kpc, for the combination of four- and two-stream data sets, respectively. The combination of four streams provides a strong lower limit, while the

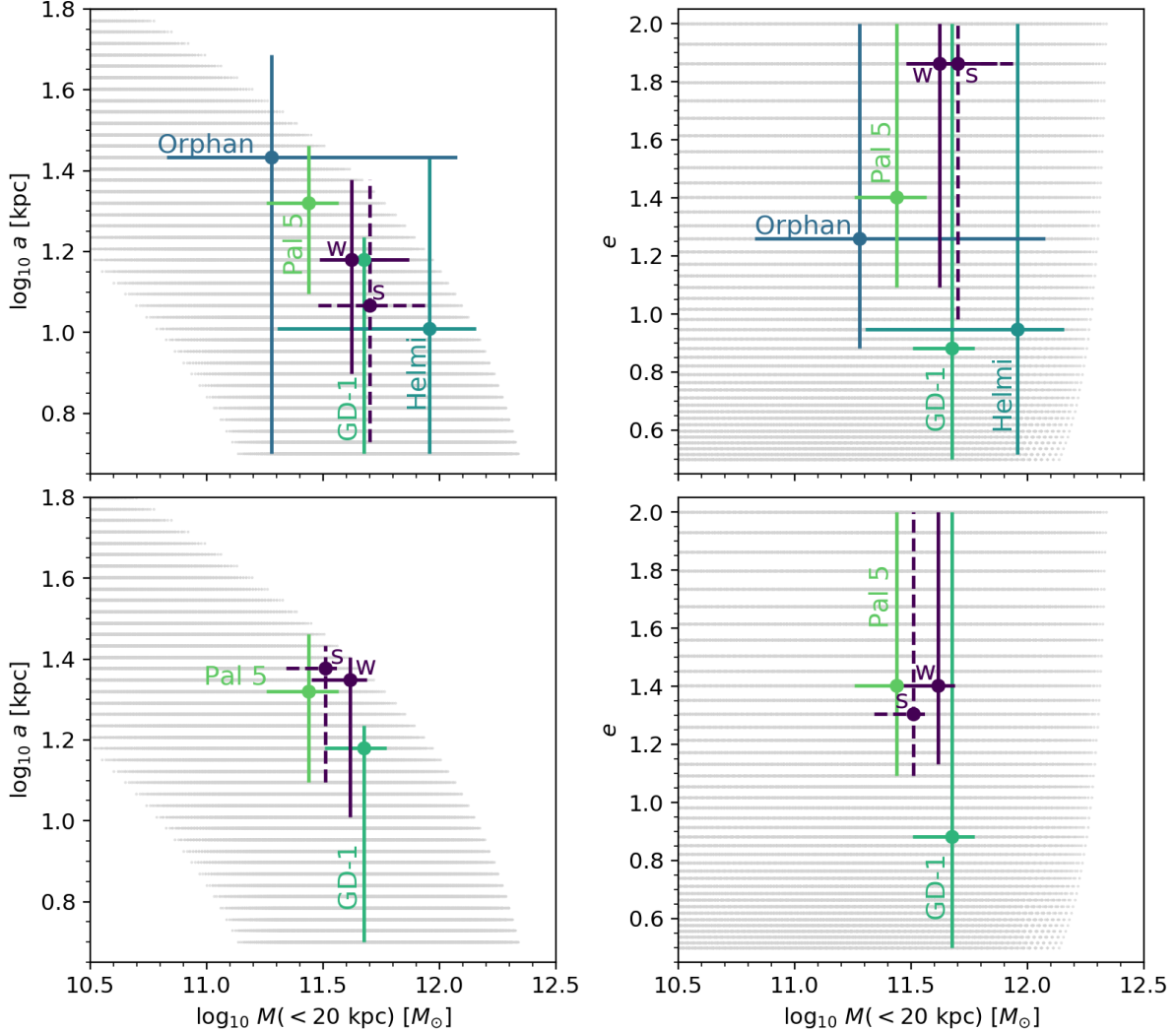


Figure 5. Comparison of best-fit parameter values for the single-component potential with their 1σ confidence intervals in enclosed mass-scale length space (left) and enclosed mass-flattening space (right). Results for individual streams are labeled with the stream name. Combined results are shown in dark purple colour and marked with an “s” and a “w” for the standard and weighted analyses, respectively. Light grey points show all considered parameter values, including those that produce unbound orbits for some stream stars. **Top:** individual stream results together with the combined *four-stream* data results. **Bottom:** individual GD-1 and Pal 5 results together with the combined *two-stream* results.

upper confidence limit is set implicitly by the maximum allowed mass for the Galaxy. On the other hand, the two-stream combination analysis yields well-defined constraints within the explored parameter space.

Although the flattening parameters of the two combinations are consistent with one another within their 1σ intervals, their best-fit values vary from 1.86 for the combination of four streams to 1.40 for the combination of GD-1 and Pal 5. These high best-fit values, which correspond to oblate potentials, are likely driven by the Pal 5 and Orphan streams, which individually disfavour the lower values of e . All individual streams accept values of flattening above 1.09, and the 1σ confidence intervals of the combined sets clearly reflect this, as both find a lower limit of ~ 1.1 .

Neither set manages to determine an upper confidence limit on the flattening. The combined stream results therefore show virtually no improvement over the individual results. We therefore conclude that we can only weakly constrain the flattening parameter with our data and this one-component potential.

We do not expect the single-component potential to be a good representation of the Milky Way’s actual gravitational field for streams whose orbits intersect the disc, such as the Helmi and Pal 5 streams. Although we give results for these streams and use them in some combined fits with this model, we caution that the best-fit parameters should not be interpreted as representing a particular component of the Milky Way’s structure. The best-fit models tend to respond to the need for a more concentrated central component (i.e. the disc) than the model will allow by increasing the total mass, leading to larger circular velocities at large radii.

Figure 4 shows the total distributions of wKLD2 for the enclosed mass and flattening parameters that result from the analysis of the combined data sets (upper panel: four stream data set; lower panel: two-stream data set). The black horizontal lines are at wKLD2 = 1.5, the value that corre-

Streams	N_*	$M(< 20 \text{ kpc}) \times 10^{11} [M_\odot]$	$a [\text{kpc}]$	e	$M_{\text{tot}} \times 10^{12} [M_\odot]$
GD-1	69	$4.73^{+1.17}_{-1.52}$	$15.12^{+2.10}_{-10.11}$	$0.88^{+1.12}_{-0.38}$	$2.65^{+0.51}_{-2.171}$
Helmi	401	$9.06^{+5.25}_{-7.04}$	$10.24^{+16.88}_{-5.23}$	$0.95^{+1.05}_{-0.43}$	$2.810^{+0.35}_{-2.49}$
Pal 5	136	$2.73^{+0.94}_{-0.93}$	$20.92^{+8.03}_{-8.48}$	$1.40^{+0.60}_{-0.31}$	$1.86^{+1.30}_{-1.18}$
Orphan	117	$1.89^{+10.03}_{-1.22}$	$27.12^{+21.54}_{-22.11}$	$1.26^{+0.74}_{-0.38}$	$2.35^{+0.81}_{-1.54}$
GD-1/Pal 5 standard	205	$3.24^{+0.55}_{-1.05}$	$23.82^{+3.30}_{-11.38}$	$1.30^{+0.69}_{-0.21}$	$2.98^{+0.18}_{-2.30}$
GD-1/Pal 5 weighted	205	$4.12^{+0.76}_{-1.30}$	$22.32^{+3.10}_{-12.08}$	$1.40^{+0.60}_{-0.27}$	$3.16^{+0.0}_{-2.40}$
GD-1/Orphan/Orphan/Pal 5 standard	723	$5.01^{+4.12}_{-2.01}$	$11.66^{+4.12}_{-6.31}$	$1.86^{+0.14}_{-0.88}$	$1.30^{+1.86}_{-0.49}$
GD-1/Orphan/Orphan/Pal 5 weighted	723	$4.18^{+3.20}_{-1.14}$	$15.12^{+8.70}_{-7.22}$	$1.86^{+0.14}_{-0.77}$	$1.47^{+1.69}_{-0.61}$

Table 2. The individual and combined stream results for a single-component potential. Best-fit parameters are given with their 1σ confidence intervals.

sponds to the 1σ confidence interval for a single-component potential. The quoted 1σ confidence intervals correspond to the parameter range on the x-axis in each panel where $w\text{KLD2} \leq 1.5$ (shown with a grey shaded region). It is clear, in both cases, that the confidence interval of the enclosed mass (a combination of the scale radius and total mass parameters) is well defined. In contrast, the flattening is only weakly constrained: only the lower limits are well defined, while the upper limits are defined by the edge of the selected grid.

Figure 5 summarises the enclosed mass, scale length and flattening results with their 1σ confidence limits as presented in Table 2. For comparison, the results from both the standard and weighted KLD analysis for combinations of streams are shown. All results are found to be consistent with each other within 1σ . We find that the difference between the best fit values of the standard and weighted methods is not significant: the results are consistent within their 1σ confidence limits. Nevertheless, the use of the stellar membership knowledge clearly affects the results. In the case of the four combined streams, this has the expected effect of lowering the best-fit enclosed mass value: the influence of the Helmi stream, that contains the largest number of stars in our sample, has now been off-set. The opposite happens for the combination of GD-1 and Pal 5, where the best-fit enclosed mass increases, because we counteract the fact that Pal 5 members outnumber those of GD-1 in our sample. On the other hand, no appreciable shift is found for the best-fit scale length and flattening between the two approaches.

5 RESULTS FOR A TWO-COMPONENT POTENTIAL

In this section we present the results of fitting the streams with the two-component Stäckel potential. The best-fit parameter values are summarised in Table 3. As for the single-component potential (Section 4.1), we focus on the KLD2 results for the confidence intervals and summarise KLD1 values associated with the best-fit parameters in Appendix B and Table B1. The analysis of the single-component model results for stream combinations showed that the difference

between the best fit values of the standard and weighted methods is not significant, so we will only discuss the weighted results from this point onward.

5.1 Results for individual stream data sets

Figure 6 presents the results of the individual streams on the enclosed mass– a_{outer} plane. The 1σ confidence intervals, again marked in orange, now correspond to potentials with $\text{KLD2} \leq 2.5$ (see Section 2.3). As was the case with the single-component potential, the GD-1 and Pal 5 streams allow for stronger constraints on the enclosed mass than the Orphan and Helmi streams do, but here the difference is even more evident. On the one hand, GD-1’s 1σ interval for the enclosed mass forms a relative narrow stripe well within the allowed parameter space of potentials producing bound orbits for all stars. In contrast, the Orphan and Helmi streams include within their 1σ confidence contour almost the entire range of explored enclosed mass values.

Compared to the single-component case, the best-fit $M(< 20 \text{ kpc})$ values are now in better agreement between individual streams, ranging from 1.91×10^{11} to $7.93 \times 10^{11} M_\odot$. As with the single-component potential, the Orphan stream returns the lowest and the Helmi stream the highest estimates of enclosed mass. All four streams accept $M(< 20 \text{ kpc})$ values from $\sim 2.6 \times 10^{11}$ up to $\sim 3.3 \times 10^{11} M_\odot$.

The mass estimates of individual streams are in good agreement with the measurements obtained with a single-component potential. The variation in the best-fit values is smaller than the 1σ confidence intervals found with the single-component model (even more so for those of the two-component model) in all cases. This is especially notable in the case of the Orphan and Helmi streams, whose best-fit values differ only by 1% and 12%, respectively, between the two models, in spite of their large error bars. The best-fit values of the GD-1 and Pal 5 streams change by 19% and 26%, respectively, between the two models.

Pal 5 is therefore the most sensitive to the change of model: this might be because Pal 5 has the smallest pericentre distance relative to the Galactic Centre, where the mass in the new inner component is concentrated. In addition, Pearson et al. (2017) have shown that Pal 5 was likely

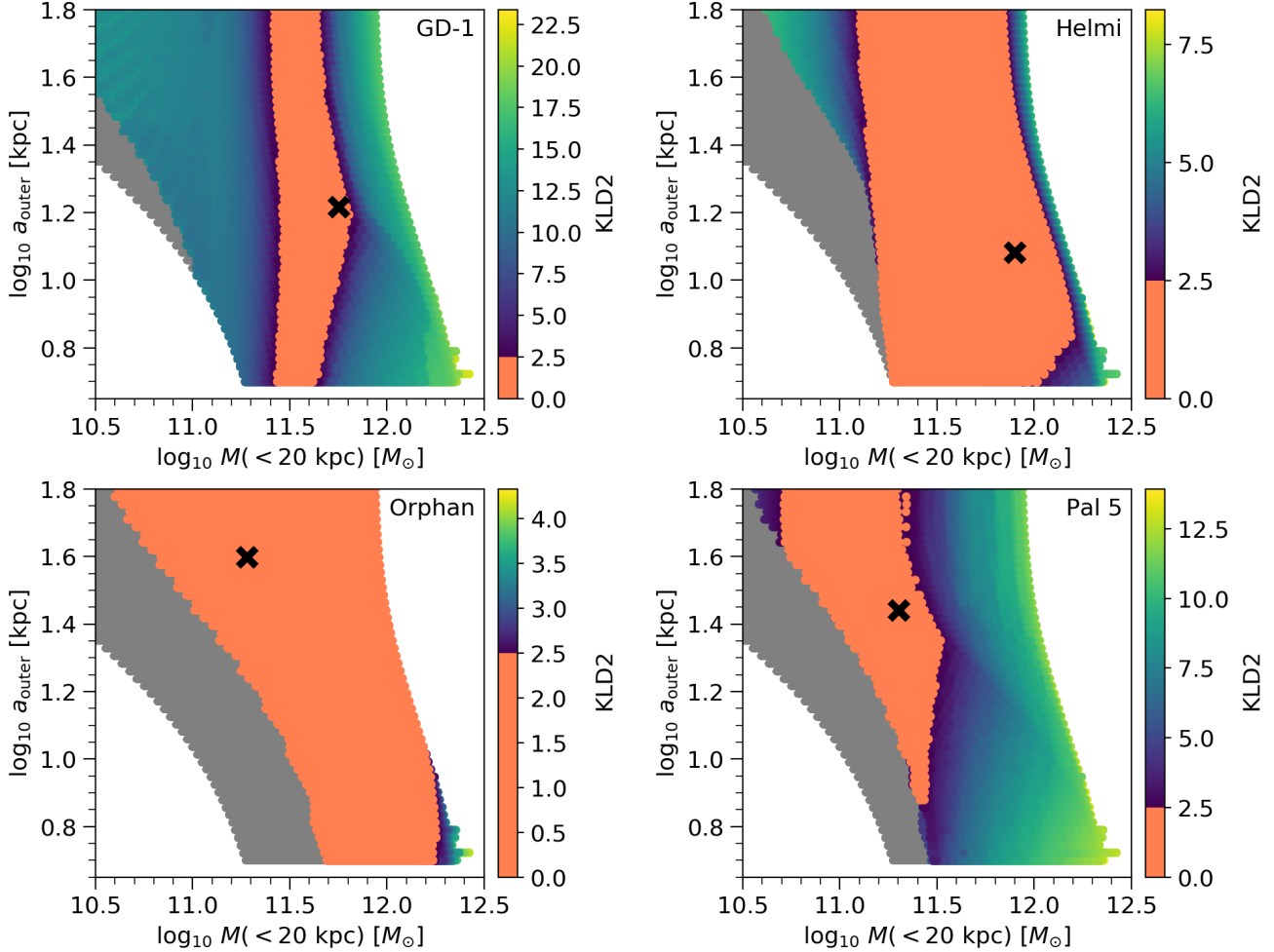


Figure 6. As in Figure 2, but showing individual stream results for the two-component potential.

affected by the Galactic bar on its pericentre passage which might add to its sensitivity to the centrally concentrated mass profile. While the Helmi stream also has a small pericentre distance, it is not as sensitive to the change in potential model. The possible reasons for this are discussed in Section 7.1.

Although all four streams have a best-fit flattening of the outer component of ~ 1 , Pal 5 data are the only ones that can actually constrain the flattening of the outer component, limiting it to be lower than 1.18. The other three streams include the entire allowed range of values within their 1σ confidence contours. The flattening of the single-component model cannot be directly compared to the flattening of the outer (or the inner) component of the two-component model. In the single-component case the flattening parameter reflects the combined axis ratios of the Galactic disc, bulge and halo. Therefore, we expect the flattening not to be spherical. In the two-component case, the two different axis ratios add more flexibility to our model, but neither of them corresponds fully to the flattening of the single-component model. We can, however, make a qualitative comparison in the case of Pal 5: the single-component model best-fit flattening is ~ 1.40 , which may be interpreted as a synthesis of the two-component results, where the outer flattening is ~ 1 , while

the inner flattening is 2.55 (as expected if the latter describes a component that incorporates a disc-like structure).

None of the other parameters can be constrained by any of the streams. As the enclosed mass is a function of all five potential parameters, we conclude that only combinations of these five parameters, but not their individual values, can be constrained.

5.2 Results for the combined data set

The results of our analysis of combined stream data sets are shown in Figure 7 in the enclosed mass - a_{outer} plane. The top panel shows the results of combining all four streams, while the bottom panel shows the results of combining just GD-1 and Pal 5.

The enclosed mass estimates of the two sets of combined results are consistent with each other within 1σ . We find $M(< 20 \text{ kpc}) = 3.12^{+5.69}_{-1.07} \times 10^{11} M_{\odot}$ for the combination of four streams and $M(< 20 \text{ kpc}) = 3.47^{+0.95}_{-1.44} \times 10^{11} M_{\odot}$ for the combination of GD-1 and Pal 5. As for the single-component potential, the GD-1 and Pal 5 combination returns confidence limits that are smaller than the limits for the four stream combination, indicating the differing biases of the individual streams participating in the fit. Notably,

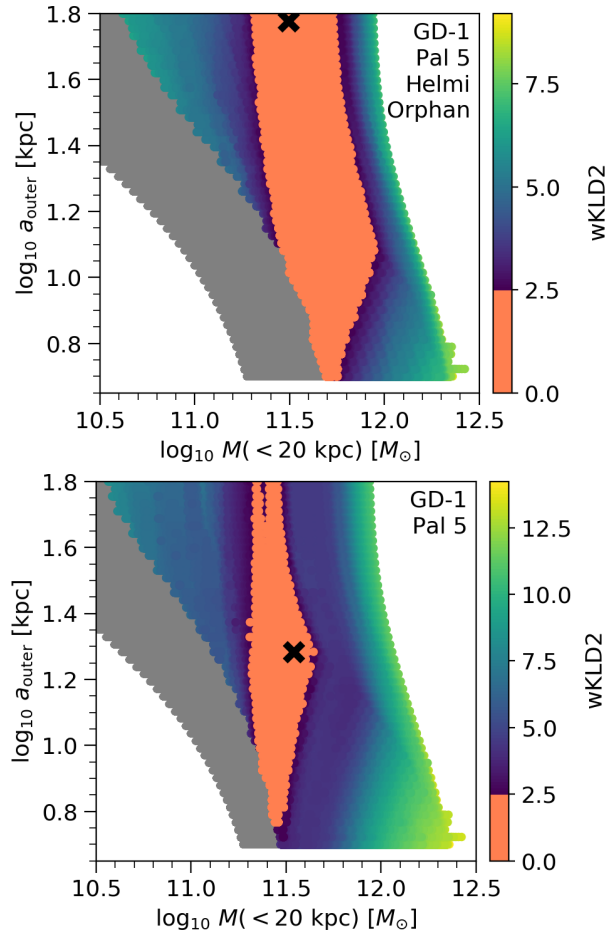


Figure 7. As in Figure 2, but showing the weighted combined data results for the two-component potential. **Top:** results for our four-stream data set. **Bottom:** results for the combination of GD-1 and Pal 5 only.

the mass estimates from combined data sets appear robust against the adopted model for the potential: they are consistent with those obtained with a single-component potential ($\sim 4.18^{+3.20}_{-1.14}$ and $\sim 4.12^{+0.76}_{-1.30} \times 10^{11} M_\odot$, respectively). The change in the best-fit estimates is 25% in the case of the four-stream combination and 16% in the case of the two-stream combination.

The analysis of the combined data sets yields slightly tighter constraints on the flattening of the outer component than the fits with individual streams: the four-stream combination places an upper limit of $e_{\text{outer}} \leq 1.71$ while the combination of GD-1 and Pal 5 limits it to ≤ 1.47 , both with a best-fit value of ~ 1 .

The other three parameters cannot be constrained with the current data. As seen from Figure 7, the limits on the scale length of the outer component are defined by the prior range. The same applies for the scale length of the inner component, the total mass and the mass ratio parameters. We conclude that it is the combinations of the five model parameters that give a fixed enclosed mass, rather than individual parameter values, that are constrained. This is illustrated quite clearly in Figure 8, which shows the total distributions of wKLD2 for the enclosed mass and the outer flattening for the combination of all four streams (upper panel) and the

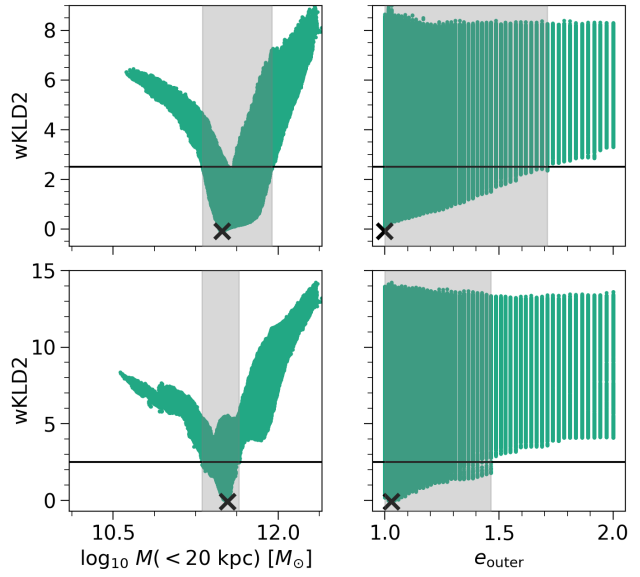


Figure 8. Weighted combined data results for the single-component potential: marginalised single parameter distributions. The positions of the best-fit parameters are marked with a black-cross. The black lines are drawn at $wKLD2=2.5$, analogous to a 1σ confidence interval (see §2.4). The light grey bars show the range of values that are accepted with $\leq 1\sigma$ confidence. **Left:** results for the four-stream data set. **Right:** results for the two-stream data set.

combination of GD-1 and Pal 5 streams (lower panel). As for the single-component case, the enclosed mass is well-constrained: the increase of the KLD2 is very steep on both sides of the best-fit value. The flattening of the outer component, on the other hand, shows a rather gentle increase of $wKLD2$ values going towards larger e_{outer} .

Figure 9 summarises the results of the two-component model as given in Table 3. Once again, all results are consistent with each other within the error bars.

6 VALIDATION

In this section we validate our results by discussing the effect of measurement errors, considering the consequences of cleaning our sample to restrict the analysis to the more informative stars, reviewing our decision to discard potentials that produce unbound stars and exploring the orbits that our results would produce for the individual streams.

6.1 Tests of fitting assumptions

To evaluate the impact that measurement errors would have on our results, we run a test with the GD-1 sample where the input positions and velocities are modified in the following manner. The observed sky positions, proper motions and radial velocities are changed by the amount of their measurement errors. The decision whether to add or subtract the error quantity is done at random for each star. The new values are assigned as the stars' current observables. The estimated distances do not have formal measurement errors, but we estimate an uncertainty of 0.5 kpc based on the spread

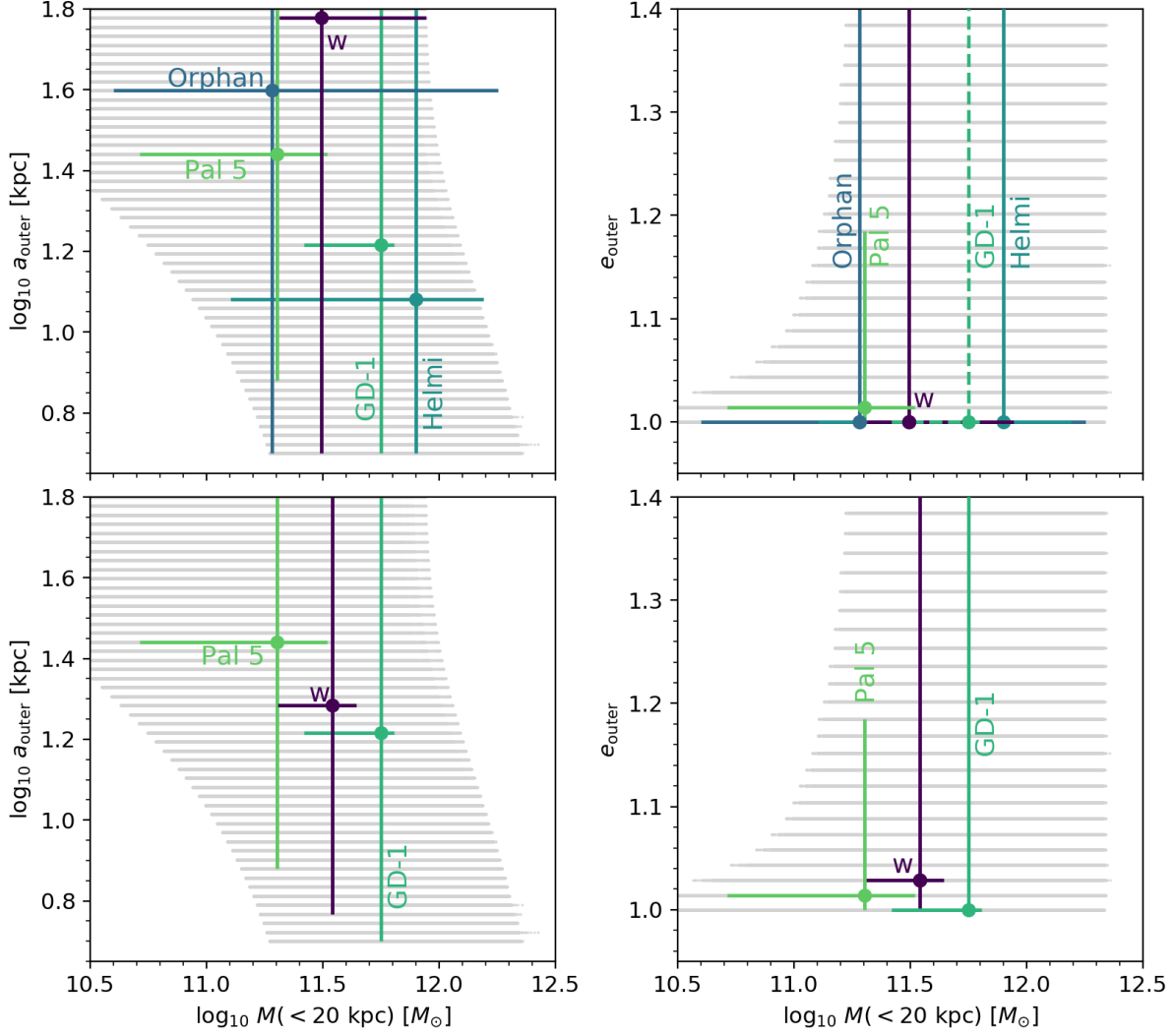


Figure 9. Comparison of the best-fit parameter values for the two-component potential with their 1σ confidence intervals in enclosed mass-scale length space (left) and enclosed mass - flattening space (right). **Top:** individual stream results together with the combined *four-stream* data results. **Bottom:** individual GD-1 and Pal 5 results together with the combined *two-stream* results. The weighted combined results are shown in dark purple colour and marked with a “w” indicator. The light grey points show all the parameter values considered, including those discarded for producing unbound orbits for stream stars.

Streams	N_*	$M(< 20 \text{ kpc}) \times 10^{11} [M_\odot]$	$a_{\text{outer}} [\text{kpc}]$	e_{outer}	$a_{\text{inner}} [\text{kpc}]$	$M_{\text{tot}} \times 10^{12} [M_\odot]$	k
GD-1	69	$5.64^{+0.75}_{-3.03}$	$16.46^{+46.64}_{-11.44}$	$1.00^{+1.00}_{-0.00}$	$4.69^{+0.32}_{-3.69}$	$3.16^{+0.00}_{-2.76}$	$0.01^{+0.29}_{-0.00}$
Helmi	401	$7.93^{+7.55}_{-6.66}$	$12.07^{+51.03}_{-7.06}$	$1.00^{+1.00}_{-0.00}$	$3.49^{+1.52}_{-2.49}$	$2.80^{+0.36}_{-2.49}$	$0.02^{+0.28}_{-0.01}$
Pal 5	136	$2.01^{+1.29}_{-1.50}$	$27.59^{+35.50}_{-20.02}$	$1.01^{+0.17}_{-0.01}$	$5.01^{+0.00}_{-4.01}$	$2.80^{+0.36}_{-2.22}$	$0.01^{+0.29}_{-0.00}$
Orphan	117	$1.91^{+16.02}_{-1.51}$	$39.62^{+23.47}_{-34.61}$	$1.00^{+1.00}_{-0.00}$	$1.53^{+3.48}_{-0.53}$	$3.16^{+0.00}_{-2.33}$	$0.04^{+0.26}_{-0.03}$
GD-1/Pal 5 weighted	205	$3.47^{+0.95}_{-1.44}$	$19.22^{+43.88}_{-13.36}$	$1.03^{+0.44}_{-0.03}$	$5.01^{+0.00}_{-4.01}$	$2.48^{+0.68}_{-1.97}$	$0.01^{+0.29}_{-0.00}$
GD-1/Orphan/Pal 5 weighted	723	$3.12^{+5.69}_{-1.07}$	$59.92^{+3.18}_{-54.91}$	$1.00^{+0.71}_{-0.00}$	$2.87^{+2.14}_{-1.87}$	$3.16^{+0.00}_{-2.33}$	$0.12^{+0.18}_{-0.11}$

Table 3. The individual and combined stream results for a two-component potential. Best-fit parameters are given with their 1σ confidence intervals.

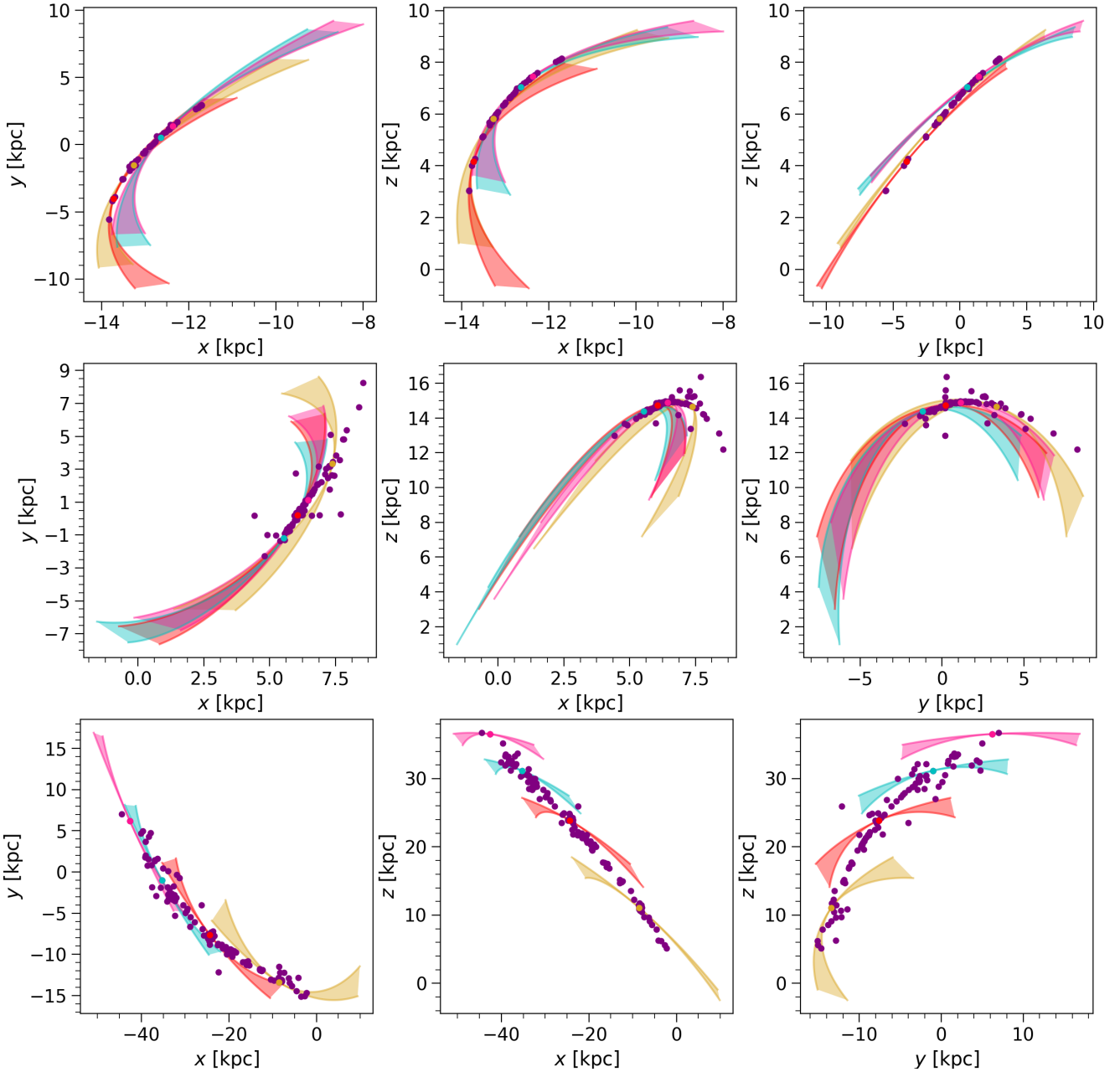


Figure 10. The orbits for the GD-1 (top), Pal 5 (middle) and Orphan (bottom) streams. These shaded regions correspond to the allowed orbits of the stars whose current position has been marked with a dot of the same colour. The edges of the shaded regions are defined by the potentials that produce the highest and the lowest enclosed mass within 20 kpc among those that are within 1σ of the best-fit results of the combined analysis of GD-1 and Pal 5 streams. Other stars in the stream are shown with purple dots. Axes are in the Galactocentric frame.

of the track measurements as shown in the top left panel of Figure 1. We add or subtract this uncertainty from the estimated distance, again selecting the sign of the perturbation randomly for each star. We transform the modified observables to Galactocentric (x, v) and repeat our analysis for the two-component potential model. The new result is consistent with the original one. The 1σ region for the enclosed mass parameter shifts only slightly compared to the original result: while previously the 1σ region encompassed values from 2.61 to $6.39 \times 10^{11} M_\odot$, with the perturbed ob-

servables it extends from 2.86 to $7.51 \times 10^{11} M_\odot$. The best-fit value itself differs by $\sim 4\%$ from the result quoted in Table 3.

To estimate the effect of cleaning up our stream sample by making selections in angular momentum, we re-analyse the GD-1 stream in the two-component potential without making any cuts to the original sample of 82 stars. The most significant change in the results is that the 1σ region for the enclosed mass has now been slightly extended. While the previous 1σ region encompasses values from 2.61 to $6.39 \times 10^{11} M_\odot$, the region resulting from the uncleaned sample contains values from 2.43 to $6.74 \times 10^{11} M_\odot$. The best-

fit value itself differs by $\sim 6\%$ from the result quoted in Table 3. This is consistent with our expectation that minor selections in constants-of-motion space to clean up outliers slightly improves the constraints but does not significantly bias the fit.

To see how our results would change when relaxing the strict condition that no stars must be unbound in acceptable potentials, we repeat our analysis for the GD-1 sample allowing for a maximum of 10% of the stars to be unbound. We find that our results for all parameters are unaffected: enforcing the strict no-unbound-stars rule does not have a significant impact.

In conclusion, none of the above mentioned choices affects our main result, the enclosed mass estimates, by more than 6 percent; all changes are far below 1σ .

6.2 Predicted orbits

Figure 10 shows the results of orbit integration using the results of the combined GD-1 and Pal 5 analysis. We track 4 stars in each of the GD-1, Pal 5 and Orphan streams. We do not show the orbits for the Helmi stream because the Helmi stream's stars are phase-mixed and do not exhibit coherent stream-like structure in position-space. Each shaded region corresponds to the star whose current position has been marked with a dot of the same colour. The edges of the shaded regions are defined by the potentials that produce the highest and the lowest $M(< 20 \text{ kpc})$ among those that are within 1σ of the best-fit potential. The Figure confirms that the orbits predicted by our analysis are locally aligned with the stream track. Importantly, the preferred range of potentials by the combined GD-1 and Pal 5 produces plausible orbits *also* for Orphan stream's stars even though Orphan's data were not used in the analysis.

7 COMPARISON AND DISCUSSION

In this section, we put our results into a broader context. We first compare our enclosed mass estimates to those obtained previously with different techniques, applied to the same stellar streams (Section 7.1). Next, we compare our results with other, more general mass estimates (see Fig. 11). Then we comment on the overall potential shape by qualitatively comparing our inferred Galactic rotation curve with recent data (Eilers et al. 2019), and with the curve obtained from the widely used potential from Bovy (2015) (Section 7.2).

7.1 Enclosed mass estimates

Our most precisely constrained parameter is the enclosed mass at 20 kpc from the GD-1 stream $5.64^{+0.75}_{-3.03} (4.73^{+1.17}_{-1.52}) \times 10^{11} M_\odot$, the Pal 5 stream $2.01^{+1.29}_{-1.50} (2.73^{+0.94}_{-0.93}) \times 10^{11} M_\odot$ and their combined data sets $3.47^{+0.95}_{-1.44} (4.12^{+0.76}_{-1.30}) \times 10^{11} M_\odot$. Here we quote our best-fit values with 1σ uncertainties for the two-component (single-component) model. The single-component accepted ranges are smaller and almost entirely contained within the two-component model accepted ranges. The relative change in best-fit

values between the two models is 19%, 26% and 16%, respectively.

Our two-component model enclosed mass estimates encompass recent mass measurements performed with independent techniques. With the orbit-fitting method, Malhan & Ibata (2019) find a mass of $M(< 20 \text{ kpc}) = 2.5 \pm 0.2 \times 10^{11} M_\odot$ with GD-1 data, while with their streakline modelling Küpper et al. (2015) obtain $M(< 19 \text{ kpc}) = (2.1 \pm 0.4) \times 10^{11} M_\odot$ using Pal 5. The latter should be compared with our $M(< 19 \text{ kpc}) = 1.81^{+1.18}_{-1.34} \times 10^{11} M_\odot$ when only Pal 5 potential is used or with $M(< 19 \text{ kpc}) = 3.16^{+0.87}_{-1.22} \times 10^{11} M_\odot$ from the combined two-stream result. We can further compare our two-stream combined results with those by Bovy et al. (2016), who derive a nearly spherical halo component with a halo enclosed mass of $M_{\text{halo}}(< 20 \text{ kpc}) = 1.1 \pm 0.1 \times 10^{11} M_\odot$. If, tentatively, we associate our outer component of the Stäckel potential with the dark matter halo we find $M_{\text{outer}}(< 20 \text{ kpc}) = 3.29^{+0.90}_{-2.23} \times 10^{11} M_\odot$. This is in agreement with the results of Bovy et al. (2016) on the low mass end which is also the case when comparing our GD-1 results with those of Malhan et al. (2018). Our results are in better overall agreement with results obtained by Küpper et al. (2015).

In contrast to the GD-1 and Pal 5 streams, both the Helmi and especially the Orphan stream stars fail to find a preferentially high clustered configuration in action space for our potential models, resulting in very poor parameter determination. Indeed, our four-stream data set manages to constrain the enclosed mass, but only because of the inclusion of GD-1 and Pal 5 data sets. We speculate that the Orphan stream may need additional complexity in the potential to reproduce its current phase-space distribution. In particular, the Orphan stream dynamics have been highly influenced by the LMC, as remarked in Sec. 3.2 and extensively discussed by Erkal et al. (2019).

There are several reasons for the strikingly weak parameter constraints provided by the Helmi stream. First, all stars in our Helmi stream sample are within the 6D *Gaia* volume, which is likely only a small segment of the whole, phase-mixed stream. A spatially limited “local sample” like this produces a subtly biased subset in action space (McMillan & Binney 2008) that could be interfering with the fit for this stream. Given its confinement to the 6D *Gaia* volume, the Helmi stream also has the most limited range of galactocentric distances of any of the streams we include in our data set. This makes it most susceptible to degeneracies between total mass and scale radius, as discussed in Bonaca et al. (2014) and Sanderson (2016). Second, the progenitor of the Helmi stream is a dwarf galaxy, which are generally hotter (in terms of their velocity dispersion) than streams from globular clusters. This means that the Helmi stream stars naturally occupy a larger volume in action space at lower density, compared to streams from globular cluster origin such as GD-1 or Pal 5, and thus have a lower maximum value of the KLD. This in turn places weaker constraints on the potential parameters. Finally, as discussed in §3, of the four streams we consider in this work, three are selected by standard observational cuts, where interlopers will likely have quite different actions (for an illustration, see Donlon et al. 2019). The Helmi stream is however identified and selected as a cluster in angular momentum space so any interlopers remaining are likely to overlap with the true stream

members in action space, also increasing the minimum size of the action-space cluster.

A visual comparison of our results with previous enclosed mass measurements is shown in Figure 11. Our mass estimates agree with most of the recent measurements, with the exception of those from Newberg et al. (2010) and Gibbons et al. (2014), while clearly also allowing for masses that are much higher.

7.2 The Galactic rotation curve

To check the global performance of our results, we calculate the resulting rotation curves for our two-component potentials (shaded areas in Figure 12) and benchmark them against the rotation curves of `galpy`'s `MWPotential2014` (Bovy 2015) (black dashed line) and McMillan (2017) (cyan dashed line) and the data from Eilers et al. (2019) (grey points). The average Galactocentric distance of the stars of each stream are marked with a dot at the rotational velocity curve of their respective best-fit potential. At those locations, we plot “error bars” given by the rotation curve values produced by potentials with KLD2 values below 2.5. This is also how the shaded uncertainty regions have been computed for all Galactocentric distances. The darker shaded regions represent the subset of these potentials that also go through the Local Standard of Rest. We have taken the rotational velocity at the Sun's location to be 232 km s^{-1} (Koppelman et al. 2018, and references therein) with an uncertainty of 10%.

The single component potentials (not shown here) do *not* provide a good match to the shape of the Galactic rotation curve: their inner rising slope is too shallow and their peaks are too far out. The two-component potentials have much more flexibility and are able to produce a realistic rotation curve. However, our uncertainties are large and we note that the overall normalisation remains somewhat high with respect to the data points from Eilers et al. (2019), which beyond $\geq 10 \text{ kpc}$ are barely included in the lower rim of the shaded region. When taking into account the additional constraint of the Local Standard of Rest velocity (marked by the red cross), we are able to further resolve the velocity curves by discarding the surplus potentials.

Finally, a related method to the one used here was proposed by Yang et al. (2020), who utilize the 2-point correlation function as a measure of clustering in the action space. They model the Milky Way potential as a combination of the disc, bulge and halo components and calculate the actions using the Stäckel fudge approximation. As opposed to this work, only the parameters of the halo component are explored while others are held fixed. They apply their method to ~ 77000 halo stars between 9 and 15 kpc with the full six-dimensional phase space information from Gaia DR2. So, although using a similar approach, they apply it to the halo stars rather than individual stellar streams as we do here. In contrast to our work, they find the best-fit circular velocity curve to be 5–10% lower than previous measurements. We think this discrepancy could be due to two factors. First, they fix the mass of the disc and bulge and fit only the halo component, but with a small range of distances the scale radius is very difficult to constrain, leading back to the total mass–scale radius degeneracy. Thus if the data prefer a slightly less massive disc/bulge their fit would naturally lead

to a lower circular velocity at higher radius, since the halo component will be less massive at the radii of the fit. Second, Yang et al. (2020) use a cutoff for the 2-point function that effectively limits the action-space size, and therefore the mass, of clusters in the distribution to structures comparable to or more massive than Gaia-Enceladus, so their clustering analysis uses essentially a completely different set of stars from ours. Therefore we do not consider it too surprising that their result differs somewhat from ours.

8 CONCLUSIONS

In this paper, we apply the action-space clustering method to known stellar stream data for the first time, and obtain constraints on the Galactic potential. Specifically, we consider members of the GD-1, Pal 5, Orphan and Helmi streams, both individually and in combination. The motivation for a simultaneous fit for multiple streams lies in obtaining more stringent, and above all robust, constraints on the mass profile over a range of Galactic distances.

Our conclusions are two-fold:

- The most *precise* constraints on the parameters are obtained with the GD-1 and Pal 5 streams. In contrast, the Orphan and Helmi streams allow a much wider range of models. We speculate why this is in section 7.1.
- Even when combining the streams that yield the most precise constraints, the only parameter we can robustly constrain is the enclosed mass, which we calculate at 20 kpc (corresponding to the mean distance for stars in our sample) for comparison across all our fits. Our best-fit estimates range between $2 - 6 \times 10^{11} M_\odot$. In particular, for a two-component potential model we find for the GD-1 stream $M(< 20 \text{ kpc}) = 5.64^{+0.75}_{-3.03}$, for the Pal 5 stream $M(< 20 \text{ kpc}) = 2.01^{+1.29}_{-1.50}$ and for their combination $M(< 20 \text{ kpc}) = 3.47^{+0.95}_{-1.44}$. The combination of all four streams in our sample yields $M(< 20 \text{ kpc}) = 3.12^{+5.69}_{-1.07}$. Our best enclosed mass results are consistent with recent measurements, obtained with the same streams.

Future developments of this work should incorporate more data from known streams, spread over a large range of Galactocentric distances and with reliable 6D information for stellar members. Moreover, our procedure, as tested here, can more broadly be applied to a large ensemble of halo stars with 6D information without knowing stream membership, as originally intended by Sanderson et al. (2015). Data to do this over a sufficiently broad distance range are within reach in the near future, thanks to upcoming spectroscopic surveys, such as WEAVE, 4MOST, DESI, and SDSSV, that will complement the increasingly precise next data releases of the ESA Gaia mission.

ACKNOWLEDGEMENTS

We thank Tim de Zeeuw for helpful comments and discussion. This work has made use of data from the European Space Agency (ESA) mission *Gaia* (<https://www.cosmos.esa.int/gaia>), processed by the *Gaia* Data Processing and Analysis Consortium (DPAC, <https://www.cosmos.esa.int/web/gaia/dpac/consortium>). Funding for

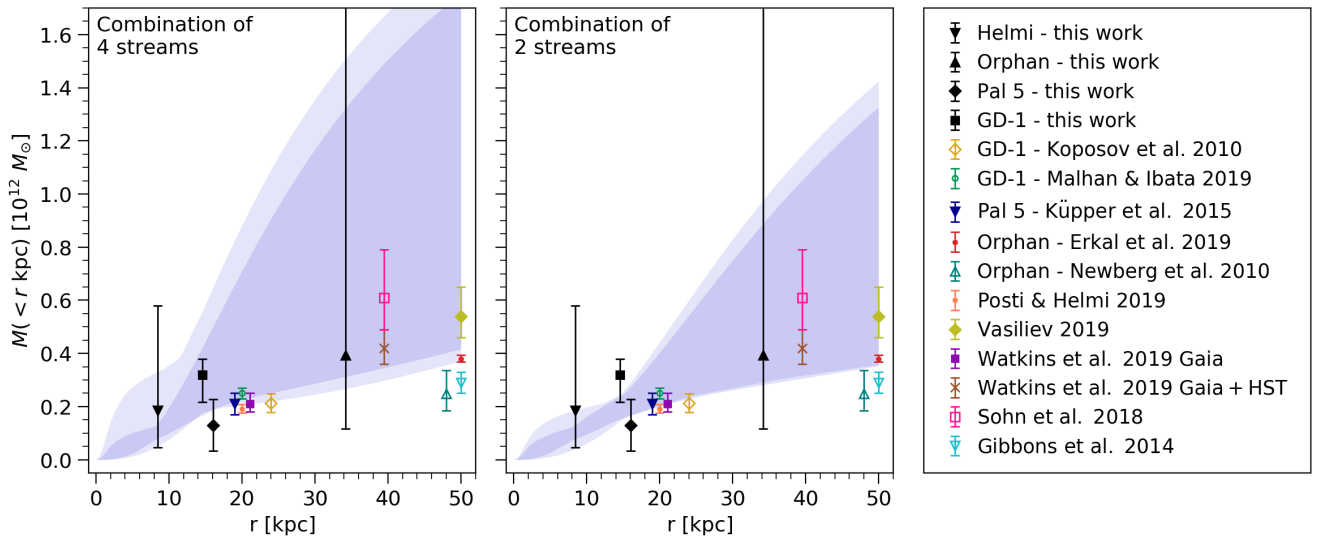


Figure 11. Comparison of our two-component potential results with previous measurements of the enclosed mass at different radii. The light blue shaded area represents the combined results for all four streams (left panel) and for GD-1 and Pal 5 (right panel). The darker shaded regions show the subset of the potentials that are compatible with the current measurements of the Local Standard of Rest velocity. The black markers signify individual stream results at their respective average radii. The coloured markers show measurements of the enclosed mass by other authors. The markers showing the results of Koposov et al. (2010) and Newberg et al. (2010) are slightly offset from 20 kpc and 50 kpc, respectively, for clarity.

the DPAC has been provided by national institutions, in particular the institutions participating in the *Gaia* Multi-lateral Agreement. This project was developed in part at the 2019 Santa Barbara *Gaia* Sprint, hosted by the Kavli Institute for Theoretical Physics at the University of California, Santa Barbara. This research was supported in part at KITP by the Heising-Simons Foundation and the National Science Foundation under Grant No. NSF PHY-1748958.

DATA AVAILABILITY

The data underlying this article are available in the article and in its online supplementary material.

APPENDIX A: DATA COLLECTION

We compile the 6D phase space data for three of the four streams used in this work (GD-1, Orphan, and Palomar 5) from various literature sources. In this Appendix we describe in detail the data assembly process for each individual stream (§ A1–A3). To convert from the assembled 6D Helio-centric observables to Galactocentric Cartesian coordinates, we further make the following assumptions:

- The Sun is located at a distance of 8.2 kpc from the Galactic Centre in the direction of the negative X-axis and 27 pc above the Galactic plane in the direction of the positive Z-axis (Chen et al. 2001).
- The Sun's peculiar velocity is $(11.1, 12.24, 7.25)$ km s $^{-1}$ (Schönrich et al. 2010).
- The velocity of the local standard of rest is 232 km s $^{-1}$ (Koppelman et al. 2018, and references therein).

A1 GD-1 data

We combine data from four literature sources to create a list of identified GD-1 members with full 6D phase space information. Koposov et al. (2010) performed spectroscopic measurements for 23 GD-1 members at the Calar Alto observatory. They also provide stream track distances, i.e. estimates of constant distance for certain intervals of the stream's track. They divide the GD-1 stream into 6 sections based on the stream-aligned longitude coordinate ϕ_1 and derive a distance to each by isochrone fitting using SDSS photometry. Willett et al. (2009) list a further 48 high-confidence GD-1 members in their Table 2. The table includes individual radial velocities as measured by the SEGUE survey, but no individual distances. Table 1 in Li et al. (2017) contains another 20 GD-1 stars with radial velocity information from LAMOST. We select only the 11 stars that were flagged by the authors as high confidence members, i.e. candidates with confidence level 1. In addition, we use the stream track distances from Li et al. (2018) Table 1, determined by fitting isochrones (i.e. using the same strategy as Koposov et al. 2010) to 18 different regions along the GD-1 stream. In total, this makes 82 candidate GD-1 members with measured radial velocities. For these stars we assemble the full phase space information in the following way:

- (i) The SDSS identifiers given in Koposov et al. (2010) Table 1 and Willett et al. (2009) Table 2 are matched with the corresponding Gaia DR2 identifiers using Simbad.
- (ii) The Gaia DR2 identifiers for these two data sets are used to acquire Gaia DR2 position and proper motion coordinates for each star.
- (iii) The candidate members in the third data set, stars with confidence level 1 in Li et al. (2017) Table 1, are cross-matched with the Gaia DR2 catalogue in TOPCAT using the LAMOST right ascension and declination with a 1 arcsec

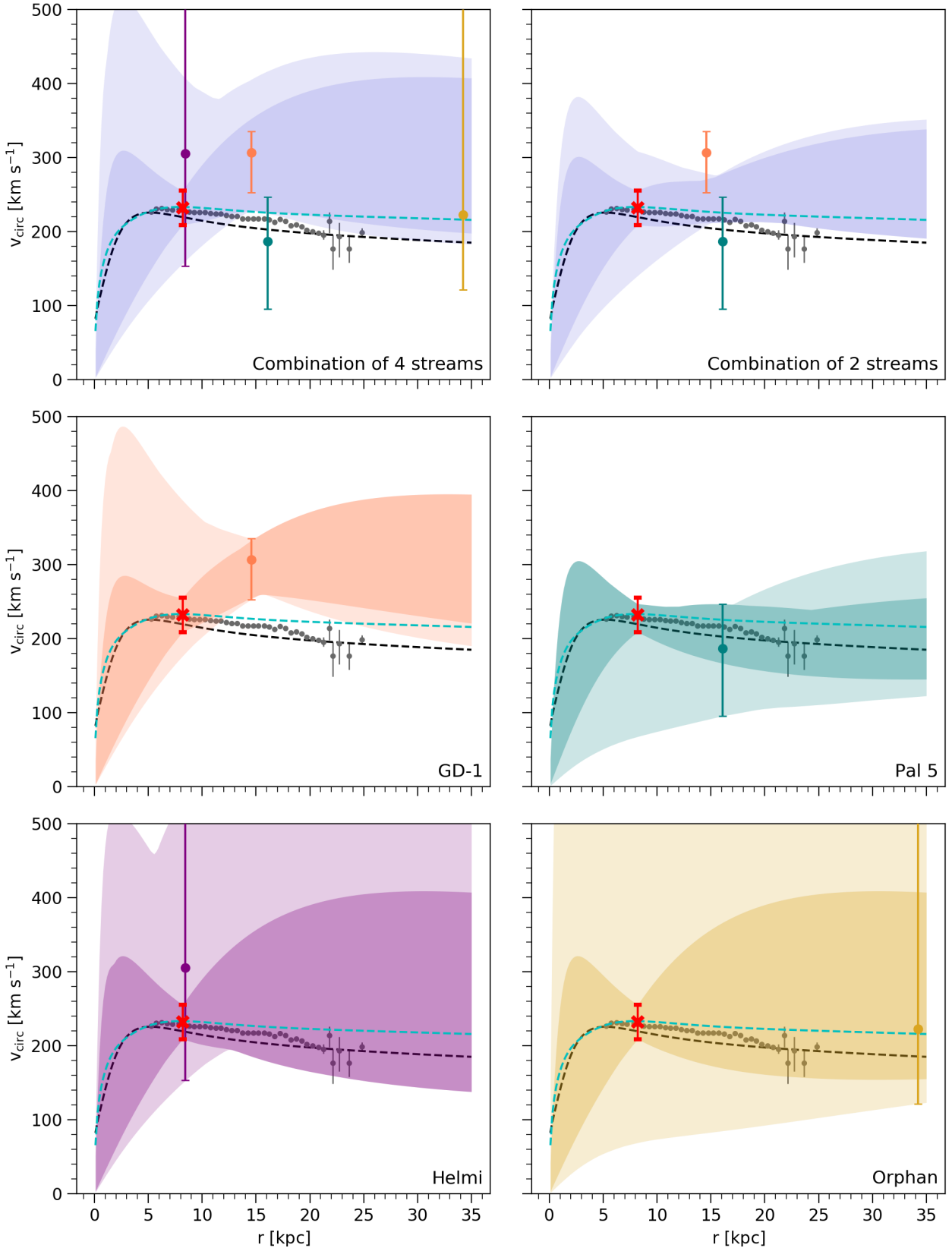


Figure 12. Rotation curves corresponding to the results of the two-component potential model. The lighter shaded region shows the rotation curves for potentials within 1σ of the best-fit for each data set. The purple, orange, teal and yellow data points correspond to the results of the Helmi, GD1, Pal 5 and Orphan streams, respectively: they show the rotation velocity of the best-fit potential at the mean Galactocentric distance of the stars in that stream. The darker shaded region shows the subset of the rotation curves that are compatible with the current measurements of the Local Standard of Rest velocity. For comparison, the dashed black and cyan lines are the rotation curves from the `galpy MWPotential2014` (Bovy 2015) and McMillan (2017), respectively, and the grey dots represent the data from Eilers et al. (2019).

search radius to find their Gaia DR2 positions and proper motions.

(iv) LAMOST radial velocities have been shown to be underestimated by 4.5 km s^{-1} (Anguiano et al. 2018). We correct for this by adding 4.5 km s^{-1} to the quoted LAMOST radial velocities.

(v) Using the transformation matrix in the Appendix of Koposov et al. (2010) the stream aligned longitude coordinate ϕ_1 is calculated using Gaia DR2 right ascension and declination for all stars.

(vi) A polynomial of degree 2 is fitted to the combined stream track distance data from Li et al. (2018) Table 1 and Koposov et al. (2010) Table 3 using the inverted measurement uncertainties as weights.

(vii) The polynomial fit is then used to find distances to each star based on their ϕ_1 values (see the top left panel of 1).

Finally, we make a further cut by discarding the 13 stars that are not part of the central clump in $L_z - L_\perp$ and $\mu_\alpha - \mu_\delta$ space.

A2 Orphan Stream data

We draw from two literature sources to build our Orphan stream members list.

Koposov et al. (2019) identify 109 likely Orphan stream members amongst the RR Lyrae stars in Gaia DR2, which are listed alongside their heliocentric distances in Table 5. The stream track distances defined according to the distribution of the RR Lyrae members are given in Table C2. In addition, the stream radial velocity track (given in the Galactic standard of rest) derived using likely Orphan stream members found in the SDSS data is presented in Table 3. We collect the 6D phase space information for these 109 members in the following way:

(i) We use TOPCAT to cross-match the stars in Table 5 of Koposov et al. (2019) with the Gaia DR2 catalogue, using a 1 arcsec search radius.

(ii) We fit a polynomial of degree 2 to the radial velocity track information from Table 3 in Koposov et al. (2019) using the inverted measurement uncertainties as weights.

(iii) The transformation matrix in Appendix B of Koposov et al. (2019) is used to find ϕ_1 for all stars.

(iv) There are no radial velocity track measurements in the negative ϕ_1 part of the stream, leading the fit in that region to be unreliable. Therefore, we neglect the 52 stars with $\phi_1 < 0$.

(v) The polynomial function is used to find a radial velocity estimate for the remaining 57 stars based on their ϕ_1 values (see the bottom right panel of 1).

(vi) Finally, since the fit to the radial velocities is done in the Galactic standard of rest frame, we transform the v_{gsr} assigned to the stream members back to the heliocentric rest frame using the solar reflex motion that Koposov et al. (2019) adopted for their transformation. This is necessary to maintain a uniform transformation of all stars from heliocentric to Galactocentric Cartesian coordinates across all samples, using consistent values for the solar position and velocity.

Li et al. (2017) present 139 Orphan stream members

with either LAMOST or SDSS radial velocities. In this work we use only the 82 highest confidence members, i.e. candidates with confidence level 1. We find the full phase space map for these stars using the following steps:

(i) We use TOPCAT to cross-match the SDSS or LAMOST right ascension and declination provided for the stars in Li et al. (2017) with the Gaia DR2 catalogue, again using a 1 arcsec search radius.

(ii) As for GD-1, LAMOST radial velocities are corrected by adding 4.5 km s^{-1} to the quoted values.

(iii) A polynomial of degree 4 is fitted to the points defining the heliocentric distance track in Table C2 of Koposov et al. (2019). We assume the measurement errors of the RR Lyrae distances from Gaia DR2 to be of order 5% and use the inverted errors as weights in the fit.

(iv) The transformation matrix in Appendix B of Koposov et al. (2019) is used to find ϕ_1 for all stars.

(v) The polynomial function is used to find a distance estimate for each star based on their ϕ_1 values (see the top right panel of 1)

A cross-match between the two data sets using Gaia DR2 source identifiers reveals 2 common stars: for these 2 stars we use distances from Koposov et al. (2019) and radial velocities from Li et al. (2017).

In summary, our data set consists of 2 stars with both radial velocity and distance measurements, 80 stars with radial velocity measurements and fitted distances, 55 stars with distance measurements and fitted radial velocities. The fitted estimates are consistent with the spread of the measurements both in the case of distances and radial velocities, as can be seen in Figure 1. Lastly, a cut in in $L_z - L_\perp$ and $\mu_\alpha - \mu_\delta$ space is performed to discard outliers. Our final Orphan sample thus consists of 117 stars.

A3 Palomar 5 stream data

We use 2 literature sources to create a list of Palomar 5 stream members with a full 6D phase space map.

Price-Whelan et al. (2019) find 27 Palomar 5 stream members in the sample of stars that appear both in the PanSTARRS-1 catalog of RR Lyrae stars (Sesar et al. 2017) and the RR Lyrae catalogs of Gaia DR2 (Holl et al. 2018), presented with derived heliocentric distances in Table 2 of Price-Whelan et al. (2019). We build a full 6D phase space map for these 27 members using the following steps:

(i) We use the Gaia DR2 source identifiers in Table 2 of Price-Whelan et al. (2019) to determine Gaia DR2 positions and proper motions for all stars.

(ii) We calculate the stream-aligned longitude coordinate ϕ_1 using the transformation matrix provided in Price-Whelan et al. (2017), applied to the Gaia DR2 right ascension and declination, for all stars.

(iii) The radial velocity track is created from measurements of individual Pal 5 stream members in Table 2 of Ibata et al. (2017). We begin by cross-matching the table with the Gaia DR2 catalogue in TOPCAT, using the right ascension and declination with a 1 arcsec search radius. We then transform to stream-aligned coordinates using the rotation matrices provided in Price-Whelan et al. (2017), and select

only the 115 stars that within $\pm 15 \text{ km s}^{-1}$ of -55.30 km s^{-1} , guided by the fit performed by Ibata et al. (2017).

(iv) A line is fitted to the radial velocities of the retained stars. We add the uncertainties of the measurements and the membership probability in quadrature and use the inverted values as weights in the fit.

(v) The polynomial function is used to find a radial velocity estimate for each star based on its ϕ_1 value (see the bottom middle panel of 1).

Ibata et al. (2017) present a sample of 154 members of the Palomar 5 stream alongside their radial velocity measurements in their Table 2. We find the full 6D phase space for these stars in the following way:

(i) A cross-match between the stars in Table 2 of Ibata et al. (2017) and the Gaia DR2 catalogue is performed in TOPCAT using the right ascension and declination with a 1 arcsec search radius. We find that not all Ibata et al. (2017) stars cross-match to a unique Gaia star: some Gaia stars are the best match for two (or in one case even three) Ibata et al. (2017) stars. If possible, in each pair we select the star that has a smaller angular distance to their Gaia match, and discard the other star. In the cases where both stars in the pair have the same angular distance to the Gaia star, we select one or the other, randomly.

(ii) Using the transformation matrix provided in Price-Whelan et al. (2017), we calculate the stream-aligned longitude coordinate ϕ_1 using Gaia DR2 right ascension and declination for all stars.

(iii) The distance track is created from Table 2 in Price-Whelan et al. (2019) by cross-matching the table with the Gaia DR2 catalogue using Gaia DR2 source identifiers and transforming to stream-aligned coordinates using the rotation matrices provided in Price-Whelan et al. (2017).

(iv) A polynomial of degree 2 is fitted to these distances. The measurement errors on the distances are of order 3% (Sesar et al. 2017). We add these uncertainties and the membership probabilities in quadrature and use the inverted values as weights in the fit.

(v) The polynomial function is used to find a distance estimate for each star based on their ϕ_1 values (Figure 1, top middle panel).

After this procedure, the two data sets are joined (there are no common stars in the two samples). Finally, we discard outliers in $L_z - L_\perp$ and $\mu_\alpha - \mu_\delta$ space. This cut reduces our final Palomar 5 sample to 136 stars.

This set of 136 stars contains 10 Ibata et al. (2017) stars that originally had a duplicate with the same angular distance to their matched Gaia star, as explained above. Although we use only one set of these duplicates in our work, we find that if we use the alternate set of 10 stars instead, our results for Pal 5 would remain virtually unchanged: for the single-component model the best-fit value changes 6% while for the two-component model there is no change to the best-fit value. In both cases the range of values that the 1σ region encompasses remains unchanged.

APPENDIX B: KLD1 EXAMPLE

Here, we briefly discuss the determination of the best fit values using the KLD1 (Equations 16 and 19). In the left panel

of Figure B1 we show a representative example of the KLD1 contours as a function of enclosed mass and scale length, for the Pal 5 stream in the single-component model. There is a clear single peak in parameter space; the best-fit model is marked with the black cross. To give an idea of the difference in clustering associated with a given difference in KLD1, we also mark another location in parameter space that has KLD1 2.16 units lower than the best fit (purple cross) for comparison. In the central panel, we show the action distribution corresponding to the best fit model (black cross), which should be the most clustered. For comparison, in the right panel, we show the action distribution corresponding to the potential with lower KLD1 (purple cross), which shows a visibly less clustered action distribution. The centroid of the cluster has also moved, which is expected since the stream will be on different orbits in the two different potentials.

Table B1 summarises the KLD1 values of the best-fit results for all streams and stream combinations. Since these values are per star, they also serve as a measure of how intrinsically clustered each stream's stars are (in the individual fits) as well as how clustered the total distribution is (for the consensus fits). We remind the reader that the higher the KLD1 value, the greater the clustering in action space.

For the individual fits, GD-1 and Pal 5 can achieve the tightest clustering across all models, while the Helmi and Orphan streams are less clustered. GD-1 and Pal 5 are thought to originate from globular clusters (in Pal 5's case the progenitor is known), while Orphan and Helmi are more likely disrupted satellite galaxies. The tighter clustering of the globular cluster streams compared to the satellite streams is consistent with the smaller total phase-space volume of globular clusters compared with satellite galaxies. The Orphan Stream is substantially less clustered than Helmi according to this measure, but this may be partially due to the localized nature of the sample of Helmi stream stars, which likely do not fully sample the phase-space volume occupied by its progenitor.

Differences between the KLD1 of consensus fits and the KLD1 for each individual stream provide some indication of the degree of tension between the best-fit potentials preferred by each stream individually. This is another way of understanding the trade off between the precision of the individual stream fits and the improved accuracy of the combined fits. When combining GD-1 and Pal 5, this tension reduces the information content per star only slightly compared to the maximum clustering of Pal 5, but quite a lot compared to the best fit for GD-1. This is sensible given that the consensus best fit (e.g. Figure 12) is somewhat closer to the Pal 5 individual best fit. However for the combined fit from all streams, there is more tension: the individual KLD1 values for three of the streams are much higher than the combination value, but are likely offset in this somewhat by the intrinsically less clustered Orphan Stream.

Finally, the difference between the best-fit KLD1 for different potentials used for the consensus fits indicates how much more (or less) clustering per star is achieved by a change to the model, allowing us to do model comparison. The Akaike (1974) Information Criterion is based on this concept, although it is usually expressed in terms of a log-likelihood. Moving from the one- to two-component model

Stream	1-comp	2-comp
GD-1	17.37	16.64
Helmi	13.43	13.43
Pal 5	14.81	13.71
Orphan	9.85	9.84
GD-1/Pal 5	14.36	-
GD-1/Pal 5 weighted	14.31	13.95
GD-1/Orphan/Orphan/Pal 5	11.57	-
GD-1/Orphan/Orphan/Pal 5 weighted	10.99	11.06

Table B1. KLD1 values for the best-fit results from individual and combined streams for single-component (1-comp) and two-component (2-comp) potentials.

produces little to no increase (and sometimes a decrease) for each individual stream and for the two-stream combined model, underlining our finding that most of the additional parameters are not well constrained. This is not so surprising given that we are trying to constrain 5 parameters with only two streams. However, a slight increase is apparent when using the four-stream combined sample, hinting that adding a few more streams may in fact provide greater constraining power for more complex models and allow us to do true model comparison with the KLD1.

REFERENCES

Akaike H., 1974, IEEE Transactions on Automatic Control, 19, 716

Amorisco N. C., 2015, *MNRAS*, 450, 575

Amorisco N. C., Gómez F. A., Vegetti S., White S. D. M., 2016, *MNRAS*, 463, L17

Anguiano B., et al., 2018, *A&A*, 620, A76

Banik N., Bovy J., 2019, *MNRAS*, 484, 2009

Batsleer P., Dejonghe H., 1994, *A&A*, 287, 43

Belokurov V., et al., 2006, *ApJ*, 642, L137

Bernard E. J., et al., 2014, *MNRAS*, 443, L84

Bernard E. J., et al., 2016, *MNRAS*, 463, 1759

Binney J., Tremaine S., 2008, Galactic Dynamics: Second Edition

Bonaca A., Geha M., Küpper A. H. W., Diemand J., Johnston K. V., Hogg D. W., 2014, *ApJ*, 795, 94

Bonaca A., Hogg D. W., Price-Whelan A. M., Conroy C., 2019, *ApJ*, 880, 38

Bonaca A., et al., 2020, *ApJ*, 892, L37

Bovy J., 2015, *ApJS*, 216, 29

Bovy J., Bahmanyar A., Fritz T. K., Kallivayalil N., 2016, *ApJ*, 833, 31

Carlberg R. G., Grillmair C. J., Hetherington N., 2012, *ApJ*, 760, 75

Chen B., et al., 2001, *ApJ*, 553, 184

Dalton G., et al., 2012, WEAVE: the next generation wide-field spectroscopy facility for the William Herschel Telescope. p. 84460P, doi:10.1117/12.925950

Dejonghe H., de Zeeuw T., 1988, *ApJ*, 333, 90

Donlon Thomas I., Newberg H. J., Weiss J., Amy P., Thompson J., 2019, *ApJ*, 886, 76

Dotter A., Sarajedini A., Anderson J., 2011, *ApJ*, 738, 74

Eilers A.-C., Hogg D. W., Rix H.-W., Ness M. K., 2019, *ApJ*, 871, 120

Erkal D., Koposov S. E., Belokurov V., 2017, *MNRAS*, 470, 60

Erkal D., et al., 2019, *MNRAS*, 487, 2685

Gaia Collaboration et al., 2018, *A&A*, 616, A1

Gibbons S. L. J., Belokurov V., Evans N. W., 2014, *MNRAS*, 445, 3788

Goldstein H., 1950, Classical mechanics

Grillmair C. J., 2006, *ApJ*, 645, L37

Grillmair C. J., Dionatos O., 2006a, *ApJ*, 641, L37

Grillmair C. J., Dionatos O., 2006b, *ApJ*, 643, L17

Grillmair C. J., Johnson R., 2006, *ApJ*, 639, L17

Grillmair C. J., Freeman K. C., Irwin M., Quinn P. J., 1995, *AJ*, 109, 2553

Harris W. E., 1996, *AJ*, 112, 1487

Helmi A., 2008, *A&ARv*, 15, 145

Helmi A., White S. D. M., de Zeeuw P. T., Zhao H., 1999, *Nature*, 402, 53

Hendel D., Johnston K. V., 2015, *MNRAS*, 454, 2472

Holl B., et al., 2018, *A&A*, 618, A30

Ibata R. A., Gilmore G., Irwin M. J., 1994, *Nature*, 370, 194

Ibata R. A., Lewis G. F., Thomas G., Martin N. F., Chapman S., 2017, *ApJ*, 842, 120

Ibata R. A., Malhan K., Martin N. F., 2019, *ApJ*, 872, 152

Johnston K. V., Zhao H., Spergel D. N., Hernquist L., 1999, *ApJ*, 512, L109

Kollmeier J. A., et al., 2017, arXiv e-prints, p. arXiv:1711.03234

Koposov S. E., Rix H.-W., Hogg D. W., 2010, *ApJ*, 712, 260

Koposov S. E., Irwin M., Belokurov V., Gonzalez-Solares E., Yoldas A. K., Lewis J., Metcalfe N., Shanks T., 2014, *MNRAS*, 442, L85

Koposov S. E., et al., 2019, *MNRAS*, 485, 4726

Koppelman H., Helmi A., Veljanoski J., 2018, *ApJ*, 860, L11

Koppelman H. H., Helmi A., Massari D., Roelenga S., Bastian U., 2019, *A&A*, 625, A5

Kullback S., 1959, Information Theory and Statistics. John Wiley & Sons

Kunder A., et al., 2017, *AJ*, 153, 75

Küpper A. H. W., Balbinot E., Bonaca A., Johnston K. V., Hogg D. W., Kroupa P., Santiago B. X., 2015, *ApJ*, 803, 80

Law D. R., Majewski S. R., 2010, *ApJ*, 714, 229

Li G.-W., et al., 2017, *Research in Astronomy and Astrophysics*, 17, 062

Li G.-W., Yanny B., Wu Y., 2018, *ApJ*, 869, 122

Li T. S., et al., 2019, *MNRAS*, 490, 3508

Malhan K., Ibata R. A., 2019, *MNRAS*, 486, 2995

Malhan K., Ibata R. A., Martin N. F., 2018, *MNRAS*, 481, 3442

Mao Y.-Y., Williamson M., Wechsler R. H., 2015, *ApJ*, 810, 21

Martin N. F., et al., 2014, *ApJ*, 787, 19

Mateu C., Read J. I., Kawata D., 2018, *MNRAS*, 474, 4112

McMillan P. J., 2017, *MNRAS*, 465, 76

McMillan P. J., Binney J. J., 2008, *MNRAS*, 390, 429

Meingast S., Alves J., Fürnkranz V., 2019, *A&A*, 622, L13

Newberg H. J., Carlin J. L., 2016, Tidal Streams in the Local Group and Beyond. Vol. 420, doi:10.1007/978-3-319-19336-6,

Newberg H. J., Willett B. A., Yanny B., Xu Y., 2010, *ApJ*, 711, 32

Odenkirchen M., et al., 2001, *ApJ*, 548, L165

Odenkirchen M., et al., 2003, *AJ*, 126, 2385

Pearson S., Price-Whelan A. M., Johnston K. V., 2017, *Nature Astronomy*, 1, 633

Posti L., Helmi A., 2019, *A&A*, 621, A56

Price-Whelan A. M., Bonaca A., 2018, *ApJ*, 863, L20

Price-Whelan A., Sipocz B., Major S., Oh S., 2017, adrn/gala: v0.2.2, doi:10.5281/zenodo.1004642, <https://doi.org/10.5281/zenodo.1004642>

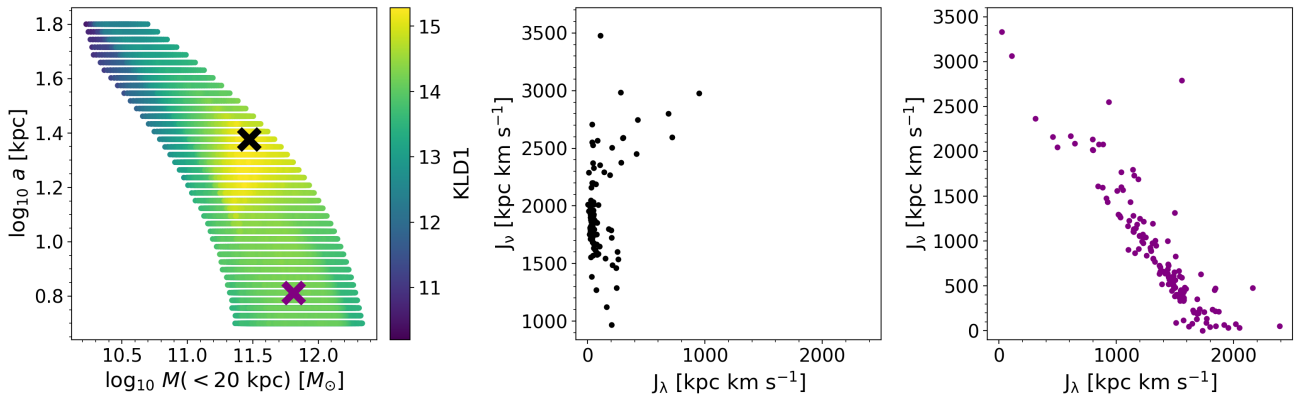


Figure B1. Comparison of action space of Pal 5 produced by two different single-component potentials. **Left:** KLD1 values as a function of enclosed mass and scale length. The higher the KLD1 value the more clustered the action-space. **Center:** action distribution of the best-fit potential (black cross in left panel). **Right:** action distribution of a different potential with KLD1 2.16 lower than the best fit (purple cross in left panel).

Price-Whelan A. M., Mateu C., Iorio G., Pearson S., Bonaca A.,

Belokurov V., 2019, *AJ*, **158**, 223

Sanders J. L., Binney J., 2013a, *MNRAS*, **433**, 1813

Sanders J. L., Binney J., 2013b, *MNRAS*, **433**, 1826

Sanders J. L., Binney J., 2016, *MNRAS*, **457**, 2107

Sanders J. L., Bovy J., Erkal D., 2016, *MNRAS*, **457**, 3817

Sanderson R. E., 2016, *ApJ*, **818**, 41

Sanderson R. E., Helmi A., Hogg D. W., 2015, *ApJ*, **801**, 98

Schönrich R., Binney J., Dehnen W., 2010, *MNRAS*, **403**, 1829

Sesar B., et al., 2017, *AJ*, **153**, 204

Sharma S., Johnston K. V., 2009, *ApJ*, **703**, 1061

Shipp N., et al., 2018, *ApJ*, **862**, 114

Sohn S. T., Watkins L. L., Fardal M. A., van der Marel R. P., Deason A. J., Besla G., Bellini A., 2018, *ApJ*, **862**, 52

Thomas G. F., Famaey B., Ibata R., Renaud F., Martin N. F., Kroupa P., 2018, *A&A*, **609**, A44

Vasiliev E., 2019a, *MNRAS*, **482**, 1525

Vasiliev E., 2019b, *MNRAS*, **484**, 2832

Vera-Ciro C., Helmi A., 2013, *ApJ*, **773**, L4

Watkins L. L., van der Marel R. P., Sohn S. T., Evans N. W., 2019, *ApJ*, **873**, 118

Willett B. A., Newberg H. J., Zhang H., Yanny B., Beers T. C., 2009, *ApJ*, **697**, 207

Yang T., Boruah S. S., Afshordi N., 2020, *MNRAS*, **493**, 3061

de Jong R. S., et al., 2019, *The Messenger*, **175**, 3

de Zeeuw T., 1985, *MNRAS*, **216**, 273

This paper has been typeset from a TeX/LaTeX file prepared by the author.